A Prompt Photon Cross Section Measurement in $\bar{p}p$ Collisions at $\sqrt{s} = 1.8$ TeV

F. Abe,[11] M. Albrow,[6] D. Amidei,[14] C. Anway-Wiese,[3] G. Apollinari,[20] M. Atac,[6] P. Auchincloss,[19] P. Azzi,[15] A. R. Baden,[8] N. Bacchetta,[15] W. Badgett,[14] M. W. Bailey,[18] A. Bamberger,[6,a] P. de Barbaro,[19] A. Barbaro-Galtieri,[12] V. E. Barnes,[18] B. A. Barnett,[10] G. Bauer,[13] T. Baumann,[8] F. Bedeschi,[17] S. Behrends,[2] S. Belforte,[17] G. Bellettini,[17] J. Bellinger,[25] D. Benjamin,[24] J. Benlloch,[6,a] J. Bensinger,[2] A. Beretvas,[6] J. P. Berge,[6] S. Bertolucci,[7] K. Biery,[16,a] S. Bhadra,[9] M. Binkley,[6] D. Bisello,[15] R. Blair,[1] C. Blocker,[2] A. Bodek,[19] V. Bolognesi,[17] A. W. Booth,[6] C. Boswell,[10] G. Brandenburg,[8] D. Brown,[8] E. Buckley-Geer,[21] H. S. Budd,[19] G. Busetto,[15] A. Byon-Wagner,[6] K. L. Byrum,[25] C. Campagnari,[6] M. Campbell,[14] A. Caner,[6] R. Carey,[8] W. Carithers,[12] D. Carlsmith,[25] J. T. Carroll,[6] R. Cashmore,[6,a] A. Castro,[15] F. Cervelli,[17] K. Chadwick,[6] J. Chapman,[14] G. Chiarelli,[7] W. Chinowsky,[12] S. Cihangir,[6] A. G. Clark,[6] M. Cobal,[17] D. Connor,[16] M. Contreras,[4] J. Cooper,[6] M. Cordelli,[7] D. Crane,[6] J. D. Cunningham,[2] C. Day,[6] F. DeJongh,[6] S. Dell'Agnello,[17] M. Dell'Orso,[17] L. Demortier,[20] B. Denby,[6] P. F. Derwent,[14] T. Devlin,[21] D. DiBitonto,[22] M. Dickson,[20] R. B. Drucker,[12] K. Einsweiler,[12] J. E. Elias,[6] R. Ely,[12] S. Eno,[4] S. Errede,[9] A. Etchegoyen,[6,a] B. Farhat,[13] G. J. Feldman,[8] B. Flaugher,[6] G. W. Foster,[6] M. Franklin,[8] J. Freeman,[6] H. Frisch,[4] T. Fuess,[6] Y. Fukui,[11] A. F. Garfinkel,[18] A. Gauthier,[9] S. Geer,[6] D. W. Gerdes,[4] P. Giannetti,[17] N. Giokaris,[20] P. Giromini,[7] L. Gladney,[16] M. Gold,[12] J. Gonzalez,[16] K. Goulianos,[20] H. Grassmann,[15] G. M. Grieco,[17] R. Grindley,[16,a] C. Grosso-Pilcher,[4] C. Haber,[12] S. R. Hahn,[6] R. Handler,[25] K. Hara,[23] B. Harral,[16] R. M. Harris,[6] S. A. Hauger,[5] J. Hauser,[3] C. Hawk,[21] T. Hessing,[22] R. Hollebeek,[16] L. Holloway,[9] S. Hong,[14] G. Houk,[16] P. Hu,[21] B. Hubbard,[12] B. T. Huffman,[18] R. Hughes,[16] P. Hurst,[8] J. Huth,[6] J. Hylen,[6] M. Incagli,[17] T. Ino,[23] H. Iso,[23] H. Jensen,[6] C. P. Jessop,[8] R. P. Johnson,[6] U. Joshi,[6] R. W. Kadel,[12] T. Kamon,[22] S. Kanda,[23] D. A. Kardelis,[9] I. Karliner,[9] E. Kearns,[8] L. Keeble,[22] R. Kephart,[6] P. Kesten,[2] R. M. Keup,[9] H. Keutelian,[6] D. Kim,[6] S. B. Kim,[14] S. H. Kim,[23] Y. K. Kim,[12] L. Kirsch,[2] K. Kondo,[23] J. Konigsberg,[8] K. Kordas,[16,a] E. Kovacs,[6] M. Krasberg,[14] S. E. Kuhlmann,[1] E. Kuns,[21] A. T. Laasanen,[18] S. Lammel,[3] J. I. Lamoureux,[25] S. Leone,[17] J. D. Lewis,[6] W. Li,[1] P. Limon,[6] M. Lindgren,[3] T. M. Liss,[9] N. Lockyer,[16] M. Loreti,[15] E. H. Low,[16] D. Lucchesi,[17] C. B. Luchini,[9] P. Lukens,[6] P. Maas,[25] K. Maeshima,[6] M. Mangano,[17] J. P. Marriner,[6] M. Mariotti,[17] R. Markeloff,[25] L. A. Markosky,[25] R. Mattingly,[2] P. McIntyre,[22] A. Menzione,[17] E. Meschi,[17] T. Meyer,[22] S. Mikamo,[11] M. Miller,[4] T. Mimashi,[23] S. Miscetti,[7] M. Mishina,[11] S. Miyashita,[23] Y. Morita,[23] S. Moulding,[2] J. Mueller,[21] A. Mukherjee,[6] T. Muller,[3] L. F. Nakae,[2] I. Nakano,[23] C. Nelson,[6] D. Neuberger,[3] C. Newman-Holmes,[6] J. S. T. Ng,[8] M. Ninomiya,[23] L. Nodulman,[1] S. Ogawa,[23]

R. Paoletti,(17) V. Papadimitriou,(6) A. Para,(6) E. Pare,(8) S. Park,(6) J. Patrick,(6) G. Pauletta,(17) L. Pescara,(15) T. J. Phillips,(5) F. Ptohos,(8) R. Plunkett,(6) L. Pondrom,(25) J. Proudfoot,(1) G. Punzi,(17) D. Quarrie,(6) K. Ragan,(16,a) G. Redlinger,(4) J. Rhoades,(25) M. Roach,(24) F. Rimondi,(6,a) L. Ristori,(17) W. J. Robertson,(5) T. Rodrigo,(6) T. Rohaly,(16) A. Roodman,(4) W. K. Sakumoto,(19) A. Sansoni,(7) R. D. Sard,(9) A. Savoy-Navarro,(6) V. Scarpine,(9) P. Schlabach,(8) E. E. Schmidt,(6) O. Schneider,(12) M. H. Schub,(18) R. Schwitters,(8) A. Scribano,(17) S. Segler,(6) Y. Seiya,(23) G. Sganos,(16,a) M. Shapiro,(12) N. M. Shaw,(18) M. Sheaff,(25) M. Shochet,(4) J. Siegrist,(12) A. Sill,(19) P. Sinervo,(16,a) J. Skarha,(10) K. Sliwa,(24) D. A. Smith,(17) F. D. Snider,(10) L. Song,(6) T. Song,(14) M. Spahn,(12) A. Spies,(10) P. Sphicas,(13) R. St. Denis,(8) L. Stanco,(6,a) A. Stefanini,(17) G. Sullivan,(4) K. Sumorok,(13) R. L. Swartz, Jr.,(9) M. Takano,(23) K. Takikawa,(23) S. Tarem,(2) F. Tartarelli,(17) S. Tether,(13) D. Theriot,(6) M. Timko,(24) P. Tipton,(19) S. Tkaczyk,(6) A. Tollestrup,(6) J. Tonnison,(18) W. Trischuk,(8) Y. Tsay,(4) J. Tseng,(10) N. Turini,(17) F. Ukegawa,(23) D. Underwood,(1) S. Vejcik, III,(10) R. Vidal,(6) R. G. Wagner,(1) R. L. Wagner,(6) N. Wainer,(6) R. C. Walker,(19) J. Walsh,(16) G. Watts,(19) T. Watts,(21) R. Webb,(22) C. Wendt,(25) H. Wenzel,(17) W. C. Wester, III,(12) T. Westhusing,(9) S. N. White,(20) A. B. Wicklund,(1) E. Wicklund,(6) H. H. Williams,(16) B. L. Winer,(19) J. Wolinski,(22) D. Wu,(14) J. Wyss,(15) A. Yagil,(6) K. Yasuoka,(23) Y. Ye,(16,a) G. P. Yeh,(6) C. Yi,(16) J. Yoh,(6) M. Yokoyama,(23) J. C. Yun,(6) A. Zanetti,(17) F. Zetti,(17) S. Zhang,(14) W. Zhang,(16) S. Zucchelli,(6,a)

The CDF Collaboration

(1) *Argonne National Laboratory, Argonne, Illinois 60439*

(2) *Brandeis University, Waltham, Massachusetts 02254*

(3) *University of California at Los Angeles, Los Angeles, California 90024*

(4) *University of Chicago, Chicago, Illinois 60637*

(5) *Duke University, Durham, North Carolina 27706*

(6) *Fermi National Accelerator Laboratory, Batavia, Illinois 60510*

(7) *Laboratori Nazionali di Frascati, Istituto Nazionale di Fisica Nucleare, Frascati, Italy*

(8) *Harvard University, Cambridge, Massachusetts 02138*

(9) *University of Illinois, Urbana, Illinois 61801*

(10) *The Johns Hopkins University, Baltimore, Maryland 21218*

(11) *National Laboratory for High Energy Physics (KEK), Japan*

(12) *Lawrence Berkeley Laboratory, Berkeley, California 94720*

(13) *Massachusetts Institute of Technology, Cambridge, Massachusetts 02139*

(14) *University of Michigan, Ann Arbor, Michigan 48109*

(15) *Universita di Padova, Instituto Nazionale di Fisica Nucleare, Sezione di Padova, I-35131 Padova, Italy*

(16) *University of Pennsylvania, Philadelphia, Pennsylvania 19104*

(17) *Istituto Nazionale di Fisica Nucleare, University and Scuola Normale Superiore of Pisa, I-56100 Pisa, Italy*

(18) *Purdue University, West Lafayette, Indiana 47907*

(19) *University of Rochester, Rochester, New York 15627*

[20] *Rockefeller University, New York, New York 10021*
[21] *Rutgers University, Piscataway, New Jersey 08854*
[22] *Texas A&M University, College Station, Texas 77843*
[23] *University of Tsukuba, Tsukuba, Ibaraki 305, Japan*
[24] *Tufts University, Medford, Massachusetts 02155*
[25] *University of Wisconsin, Madison, Wisconsin 53706*

Abstract

The first prompt photon measurement from the CDF experiment at the Fermilab $p\bar{p}$ Collider is presented. Two independent methods are used to measure the cross section, one for high transverse momentum (P_T) and one for lower P_T. Comparisons to various theoretical calculations are shown. The cross section agrees qualitatively with QCD calculations but has a steeper slope at low P_T.

Contents

List of Figures

List of Tables

1 Overview of the Physics, Detector and Methods

1.1 Prompt Photon Physics

Prompt photon production in hadronic interactions provides a test of Quantum Chromodynamics (QCD) [1, 2, 3] and a constraint on parton distributions [4, 5, 6, 7, 8, 9, 10, 11]. The differential cross section for prompt photon production has been used by experiments to extract a gluon distribution [12]. The high center of mass energy of the Tevatron allows us to test QCD and probe the gluon distribution at high momentum transfer in a previously unexplored range of $x_T = 2P_T/\sqrt{s}$ ($.016 < x_T < .070$) where gluons are the dominant partons. This process is complementary to deep inelastic scattering and to the hadronic production of W and Z bosons and jets. Since the photon's energy and direction can be measured with no uncertainties induced by hadronization, this process has an advantage over jet production measurements, especially at low transverse momentum.

This topic has been well explored theoretically[13, 14, 15, 16, 17]. The leading order diagrams for photon production in $p\overline{p}$ collisions are indicated in Fig. 1. The dominant leading order diagram for low and intermediate energy photon production is the first diagram in this set, the Compton diagram. As a consequence the cross section is sensitive to the gluon content of the proton. The other leading order diagram is $q\bar{q}$ annihilation, shown in Fig. 1b. Next-to-leading order QCD calculations have been performed for the prompt photon cross section; two NLO diagrams are shown in Fig. 1c, the left one an example of initial state gluon radiation, the right one final state gluon radiation. Figure 1d shows two examples of prompt photons associated with jets, the *bremsstrahlung* process. The left diagram calculated with perturbative QCD, has colinear singularities which are absorbed into the photon fragmentation function in the right diagram. In the *bremsstrahlung* process the photon is produced with nearby hadrons and the experimental isolation cut is an important consideration.

1.2 Prompt Photon Detection

Throughout this article the term prompt (or direct) photons is used to indicate photons produced in the initial hadronic collision in contrast to those produced by decays of hadrons like π^0 and η mesons. The CDF detector is best equipped to measure prompt photons which are *isolated* (not accompanied by a large amount of nearby energy), and an explicit isolation cut is used in this measurement. The signal-to-background ratio is enhanced by the isolation cut. Since π^0 and η mesons are produced in jets, requiring isolation greatly reduces hadronic backgrounds. This cut suppresses (but does not eliminate) the portion of the cross section that comes from the *bremsstrahlung* process, which is beneficial since this process is not well understood theoretically.

Even narrowing the class of events to those with a well isolated photon candidate leaves a substantial number of events with hadrons that 'fake' a single prompt photon. To measure the prompt rate requires one or more methods to evaluate this non-prompt background rate. The CDF experiment had two statistical methods available for the data taken during

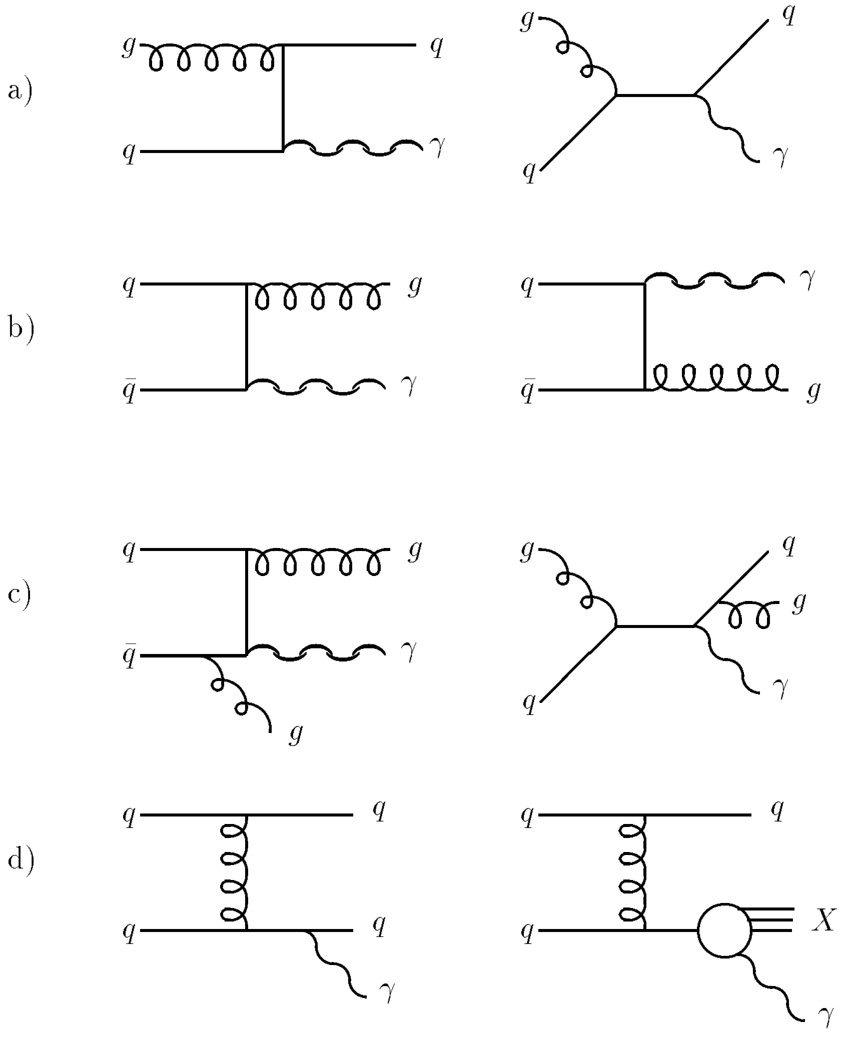

Figure 1: a) Leading order Compton QCD diagrams for prompt photon production, b) leading order annihilation diagrams, c) two next-to-leading-order diagrams, and d) two examples of photon *bremsstrahlung*, a perturbative QCD part (left) and a part using a photon fragmentation function (right).

the 1988-89 collider run. Both methods depend on the fact that the photons from hadron decays are accompanied by one or more additional photons. One method, the profile method, uses measurements of the transverse profile of the electromagnetic shower in the calorimeter to quantify the fraction of events with single photon showers. The second method, the conversion method, depends on the fact that multiple photons are more likely to produce an e^+e^- pair in a thin layer of material than a single photon.

1.3 The CDF Detector

The CDF detector is described in detail elsewhere[18]. We describe briefly some of the detector systems which are particularly important for the measurements discussed here. The most important components of the CDF detector for this analysis are the central calorimeters and tracking chambers. Throughout this discussion we use a coordinate system with z along the direction of the proton beam and with $z = 0$ at the nominal $p\overline{p}$ crossing point. The polar angle θ refers to the angle from the proton direction and r and ϕ are the distance from the beam line and the azimuthal angle, respectively. Pseudorapidity, η, is defined by the expression $\eta = -\ln(\tan\theta/2)$.

Figure 2 shows a portion of the CDF central detector. At the heart of the detector is a pair of tracking chambers used for reconstructing charged particle tracks. The vertex time projection chamber is used for obtaining the event interaction point and for providing tracking coverage beyond the central region of the detector, and the central tracking chamber (CTC) provides the high resolution, long lever arm measurement needed to reconstruct charged track momenta from their bend in the 1.41 Tesla solenoidal magnetic field[19, 20]. Just outside of the central tracking chamber there are three layers of central drift tubes (CDT) that are used for additional charged track $r-\phi-z$ determination[21].

The CDT array is made of three layers of 1.27 cm diameter stainless steel drift tubes, each 3 meters long[21]. The ϕ coordinate is determined by the pulse timing information, while the pulse height information determines the z coordinate along the tube by charge division. Photons from the interaction vertex pass through a cylinder of aluminum 9.3% of a radiation length thick, the central tracking chamber wall, before reaching the CDT. In addition the initial two layers of the CDT act as an 8.5% radiation length thick converter for the last layer. The existence of this material allows us to use the conversion rate prior to the third layer to determine the relative mix of single photon and multiple photon (background) events.

The central electromagnetic calorimeter is a conventional lead-scintillator type calorimeter with shifter bars for light collection[22]. The calorimeter is segmented into 48 independent *wedge* modules. The full central detector is constructed of two rings of 24 wedges each that make contact at $z = 0$. Each wedge subtends 15^o in azimuth and approximately one unit in η. The wedges are segmented along η into 10 projective towers, with $\Delta\eta$ approximately 0.1 for each tower. Each tower is read out independently by a pair of phototubes. The resolution of this calorimeter is $\left(\frac{\sigma_{E_T}}{E_T}\right)^2 = \left(.135/\sqrt{E_T}\right)^2 + (.02)^2$ (where $E_T = E\sin\theta$ and E is the energy measured in GeV) for electrons. Imbedded in the calorimeter at 5.9 radiation

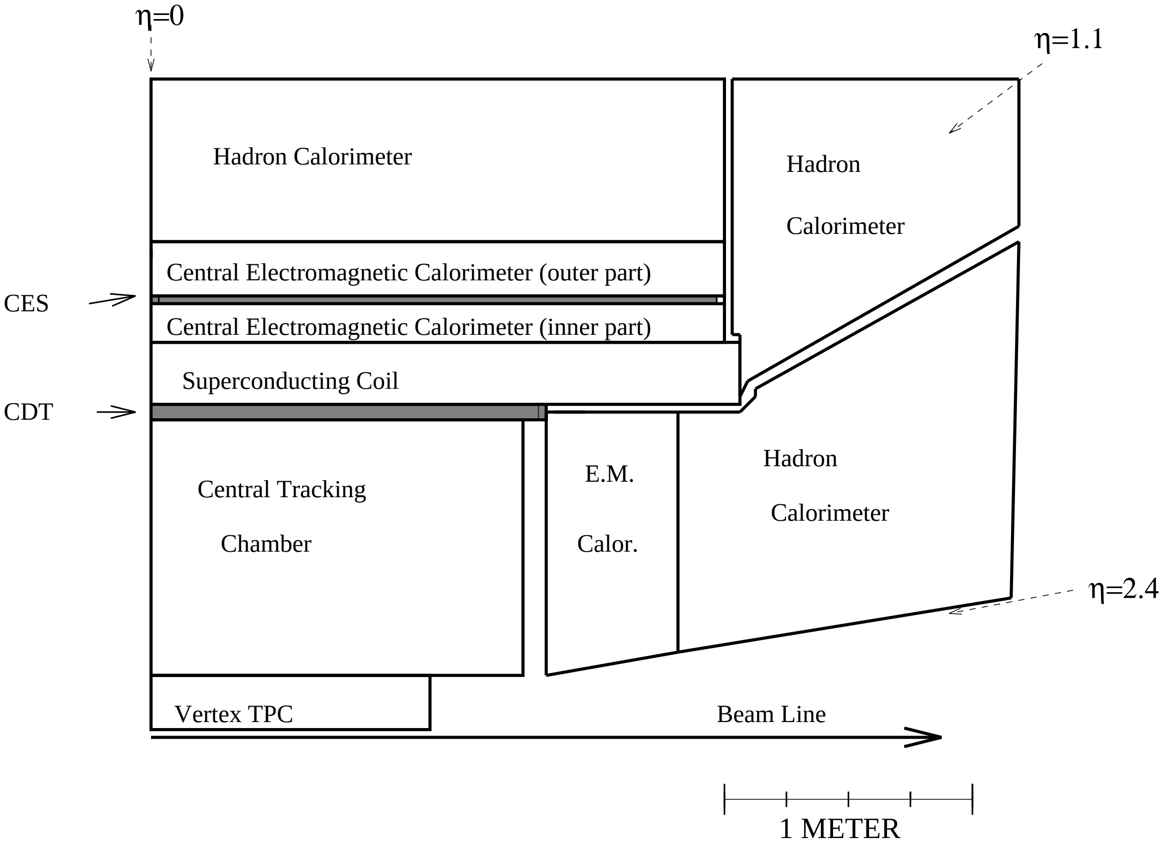

Figure 2: Cross sectional view of one quadrant of the CDF central detector.

Table 1: Central Electromagnetic Calorimeter Strip Chamber Dimensions

Perpendicular distance to beamline	184 cm
Chamber section 1	6.2 cm< $\lvert z\rvert$ <121.2 cm
Wire readout (ganged in pairs)	32 pairs $\times$ 1.45 cm
Strip readout	69 strips $\times$ 1.67 cm
Chamber section 2	121.2 cm< $\lvert z\rvert$ <239.6 cm
Wire readout (ganged in pairs)	32 pairs $\times$ 1.45 cm
Strip readout	59 strips $\times$ 2.01 cm

lengths is a gas multiwire proportional chamber with strip readout along the beamline and wire readout in azimuth. These *strip chambers* are segmented into two halves in z. The readout configuration and segmentation are indicated in table 1. The minimum separation at this chamber of a pair of photons from the decay of a π^0 with 20 GeV of transverse energy produced in a beam-beam collision is 2.5 cm, to be compared with the channel spacing in this chamber of 1.45 cm to 2.01 cm.

2 Prompt Photon Detection

2.1 Backgrounds from Neutral Meson Decays

Two largely independent methods were used to measure the prompt signal. Both methods rely on a cut and the predicted efficiency of that cut for both signal and background (given by ϵ_γ and ϵ_b). The efficiency of this cut in the data, ϵ, is then measured, and the number of signal events, N_γ is determined from the following formula (where $N_{\rm total}$ = the total number of events in the sample):

$$N_\gamma = \frac{(\epsilon - \epsilon_b)N_{\rm total}}{(\epsilon_\gamma - \epsilon_b)}. \tag{1}$$

Equation 1 comes from $\epsilon N_{\rm total} = \epsilon_\gamma N_\gamma + \epsilon_b N_B$ with $N_B = N_{\rm total} - N_\gamma$.

The first method, *the transverse shower profile method*, relied on the fact that at lower P_T, even for the decay photons from low mass states like the π^0, the transverse shape of the showers measured in the calorimeter strip chamber is different from that due to single photon showers. The second method, *the conversion method*, used the rate at which candidate events produce conversions in the material in front of the third CDT layer. Since multiphoton hadronic backgrounds convert more readily than single photons, this too can be used to evaluate the background.

2.2 Transverse Shower Profile Method for Determining Background

The prompt-photon events have a single isolated photon shower in the calorimeter. The background is composed of multiple photon showers with some spatial separation. The essence of the transverse shower profile method is to identify a class of events whose measured profiles are unlikely to be produced by a single shower. For a large enough sample of events consisting of both single showers and π^0 induced showers it is possible to evaluate the fraction of π^0 events by observing the number of showers that are 'too broad' to be consistent with a single electromagnetic shower. The number of π^0 showers that are indistinguishable from single photons can be inferred from the measured number of 'broad' showers using the characteristics of the decay and of the detector.

The dimensions of the detector and the shower sizes do not allow for a particle by particle identification. As an example, take the case of a π^0 that originates at the nominal collision vertex and decays to two photons. The minimum separation of these two photons at the strip chamber is approximately $\frac{50\ cm\ GeV/c}{P_T}$. The Moliere radius of the calorimeter lead plus scintillator is 3.5 cm which leads to shower sizes of this order at the position of the chamber. For P_T values above 15 GeV/c it is not usually possible to resolve the individual showers from the two photons from π^0 decay.

In order to evaluate at what level a single shower is consistent with the observed strip chamber data, the chamber energies were clustered and each view of the shower was fit to a standard profile (one for the wire data and one for the strips). The clustering algorithm was a simple 11 wire (or strip) window placed around a seed wire (or strip). All wires (or strips) that were above 0.5 GeV were seed candidates, and these were energy ordered. The clustering began with the highest energy seed candidate, and continued through all candidates, with the elimination of wires (or strips) used in previously found clusters. The shower fit was then performed over the 11 wires and 11 strips for each cluster. The overall energy sum of the cluster was normalized to 1.0 so the fit only depended on the relative pulse heights of the channels. The fitting procedure was optimized using test beam electrons with energies in the range 10 GeV to 100 GeV. The profile was observed to be roughly independent of energy. An approximate Chi squared per degree of freedom (referred to here as $\tilde{\chi}^2$) was developed that was independent of energy. The quantity was given by the expression:

$$\tilde{\chi}^2 = \frac{(\tilde{\chi}^2_S + \tilde{\chi}^2_W)}{2}, \tag{2}$$

where the individual contributions from the strips (wires), $\tilde{\chi}^2_{S(W)}$ are given by:

$$\tilde{\chi}^2_{S(W)} = \sum (p_i - y_i)^2 / \widetilde{\sigma_i}^2 \tag{3}$$

$$\widetilde{\sigma_i}^2 \equiv 4\left((.026)^2 + (.096)^2 y_i\right) \times \left(\frac{10 \text{ GeV}}{E}\right)^{.747}. \tag{4}$$

The p_i are the measured strip (wire) pulse heights (normalized to a total pulseheight of unity) and the y_i are the expected pulse heights. The forms for the y_i and $\widetilde{\sigma_i}^2$ were determined empirically from test beam data.

In order to model the effects of multiple showers in the calorimeter a simulation program was developed that used data from an independent set of electron test beam runs (not the ones used to tune the above parameters). Showers were scaled, translated and superimposed in a fashion appropriate to mimic the experimental conditions, while preserving all of the fluctuations (including correlations) characteristic of actual electromagnetic showers. As an illustration of the distribution in $\tilde{\chi}^2$ expected for prompt photons and π^0 background Fig. 3 shows the distributions expected from the simulation for each at P_T of 15 GeV/c.

As mentioned earlier, the number of signal events is determined from equation 1. For the profile method the efficiencies are defined to be the number of events with $\tilde{\chi}^2$ less than 4 divided by the number of events with $\tilde{\chi}^2$ less than 20. The signal $\tilde{\chi}^2$ efficiency ϵ_γ and background $\tilde{\chi}^2$ efficiency ϵ_b are estimated with the simulation. This coupled with the measurement in the data, ϵ, determines the number of photons, N_γ.

Because of the low mass of the π^0, which is a dominant background to isolated prompt photons, the technique outlined above is not useful at higher P_T. The two photons from the decay of the π^0 are almost always too close to observe a significant broadening of the shower in these events. For this reason the profile method is used only up to a P_T of 40 GeV/c.

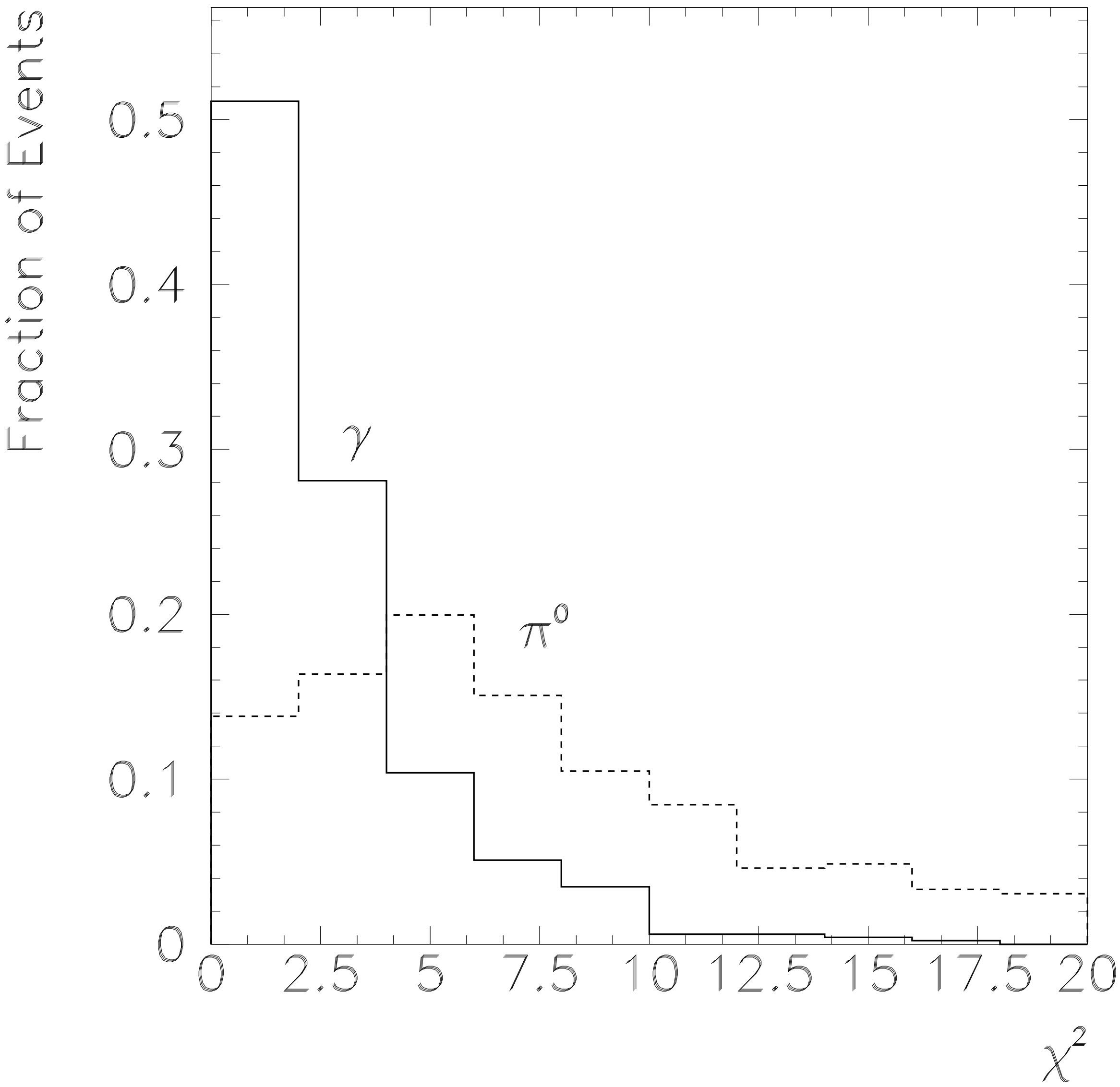

Figure 3: Simulated $\tilde{\chi}^2$ distributions for 15 GeV/c photons (solid) and π^0's (dashed).

2.3 The Conversion Method

A technique that is approximately independent of P_T has been used in the past[23]. By observing the rate at which candidates (photon or background) convert in a thin layer of radiator, the number which are single photons can be deduced. This relies on the fact that single photons have only one chance to pair produce, while multiple photons have more. The conversion rate is thereby a function of the single to multiple photon fraction. The rate of pair production for photons above 1 GeV is essentially energy independent. If the number of photons per background candidate is well known then the conversion rate predicts the background level.

The CDT system described above, while not ideal for this purpose due to the small amount of radiator in front of it, can serve to measure conversions. The conversion probability of a single photon is $\approx 10\%$, and is denoted by ϵ_γ for this method also. For two photon backgrounds the background efficiency is given by: $\epsilon_b = 2\epsilon_\gamma - \epsilon_\gamma^2$. The measured ϵ is $N_{\rm CDT}/N_{\rm total}$, where $N_{\rm CDT}$ is the number of events with a conversion measured in the CDT. The number of photons is given by equation 1.

3 Trigger and Event Selection

The sample of events used in this analysis came from a set of four CDF triggers used for data taking during the 1988-89 Fermilab collider run. Each of the triggers consisted of four levels. In order to be selected an event had to fire at least one forward and one backward beam-beam counter in coincidence (level 0). The beam-beam counters are small-angle scintillation counters that subtend a pseudorapidity of 3.24 to 5.90. The event passed the next level of trigger (level 1) if it had more than 6 GeV total in transverse energy (E_T) in trigger towers with greater than 4 GeV each in the electromagnetic calorimeter. Trigger towers subtend .2 units in rapidity and 15 degrees in ϕ.

The level 2 trigger system clustered the energy observed in the electromagnetic calorimeter[24]. This clustering started with every trigger tower that had E_T over 4 GeV. The adjacent towers in η and in ϕ were tested to see if they had E_T in excess of 3.6 GeV. If they did, they were added to the cluster and their nearest η and ϕ neighbors were likewise tested. This process continued until there were no additional towers to add to the cluster. In order to suppress charged hadron background, at least one cluster was required to be above an E_T threshold and have the ratio of total energy over electromagnetic energy less than 1.125. Two thresholds were used; A threshold of 10 GeV was applied with a variable prescaling factor to allow fewer events to be taken during high luminosity runs, and a threshold of 23 GeV was used with no prescale. Events that satisfied either of these level 2 triggers were read into the level 3 microprocessor farm.

In the level 3 processors, the clustering was done in a manner similar to the offline algorithm, which proceeded as follows. For the central calorimeter, electromagnetic towers with more than 3 GeV of energy were ordered in descending E_T and combined with their nearest neighbors in pseudorapidity provided the neighbor had more than .1 GeV. In this way from one to three towers were grouped together in clusters. These clusters (EM clusters) were required to carry at least 5 GeV of total E_T and to have less than 12.5% of this clustered electromagnetic energy observed in the hadronic towers behind them.

The events read into the level 3 farm were tested against two sets of requirements. For each of the above thresholds there was a highly isolated sample and a sample with less restriction on nearby energy, but tighter requirements on the consistency of the electromagnetic calorimeter data and what would be expected from a single electromagnetic shower. There was a significant amount of overlap between these two samples in each threshold category.

For both thresholds the highly isolated trigger required that less than 15% additional energy (compared to the EM cluster) was present in calorimeter towers whose centers fell inside of a cone given by $R = 0.7$ where $R = \sqrt{\Delta\eta^2 + \Delta\phi^2}$ is the distance in $\eta - \phi$ space from the energy centroid of the EM cluster. Since the calibration and pedestal subtraction were rough at this stage of processing, only towers with more than .25 GeV were included in the sum.

A second trigger for each of the thresholds required the same level of isolation (15%) but in a smaller cone ($R = 0.4$). This was supplemented by requiring that the energy shared across η tower boundaries in the EM cluster was consistent with that expected for a single electromagnetic shower. An energy sharing quantity known as $L_{\rm shr}$ was used to determine this. It was simply the observed leakage minus the expected divided by the square root of the EM cluster energy (all energies in GeV). There are two such quantities for three tower clusters and only one for two tower clusters. Single tower clusters are simply accepted, while multi-tower clusters are rejected if any of these quantities exceed 0.2. Figure 4 shows the distribution of this quantity ($L_{\rm shr}$) for electrons from W decay. For the lower threshold data an additional requirement was applied to the profile observed in the strip chamber. The $\tilde{\chi}^2_S$ of a single shower fit to the strip profile was required to be less than 25. Both of these requirements were very weak, but helped to reduce the number of background events from photon rich jets.

The efficiency of the low and high threshold triggers have been obtained by comparing independent trigger rates. The high threshold trigger efficiency has been obtained by comparing to the low threshold one and the low threshold trigger has been compared to a dielectron trigger with a lower threshold. The E_T dependence of the trigger efficiency is plotted in Fig. 5. These plots do not include the physics dependent loss due to the application of an isolation cut in the trigger.

3.1 Event Selection

The photon candidates were selected by offline analysis similar to that described above. EM clusters were formed using the same method as that used in the level 3 trigger. The candidate clusters were required to have less than 2.0 GeV transverse energy in a cone of $R = .7$ around them. See Fig. 6 for the distribution of E_T in a randomly placed cone for minimum bias events (events taken with no trigger except for a beam-beam counter coincidence). This represents an approximate underlying cone E_T expected for the direct photon events.

In addition, the events were required to have usable strip chamber data. The shower had to be well contained in the calorimeter, where the whole shower profile was measured. A fiducial cut was performed requiring the fitted position of the most energetic shower associated with the cluster to be within 17.5 cm of the chamber center in the direction perpendicular to the wires (i.e. in the azimuthal direction) and to have 14 cm $< |z| <$ 217 cm. In order to avoid using events in which the projective geometry of the detector is particularly unsuitable, events with a vertex more than 50 cm away from the nominal vertex position were rejected.

Events were eliminated if they had a second strip chamber cluster in the same wedge as the photon with more than 1 GeV. This cut provides significant rejection against multiple photon backgrounds. The efficiency of this cut depends on the energy of the photon candidate, as shown in Fig. 7. This shows the measurement of this efficiency for testbeam electrons, and for electrons from W boson decay (both simulated and measured). The electrons from W decay have a lower efficiency than the extrapolation from the testbeam electrons due to the radiation of an extra photon in this physics process. This radiation is present in the W simulation, and the agreement illustrates how well the detector simulation produces such low energy extra clusters. Events were also eliminated if the single shower fit to their strip

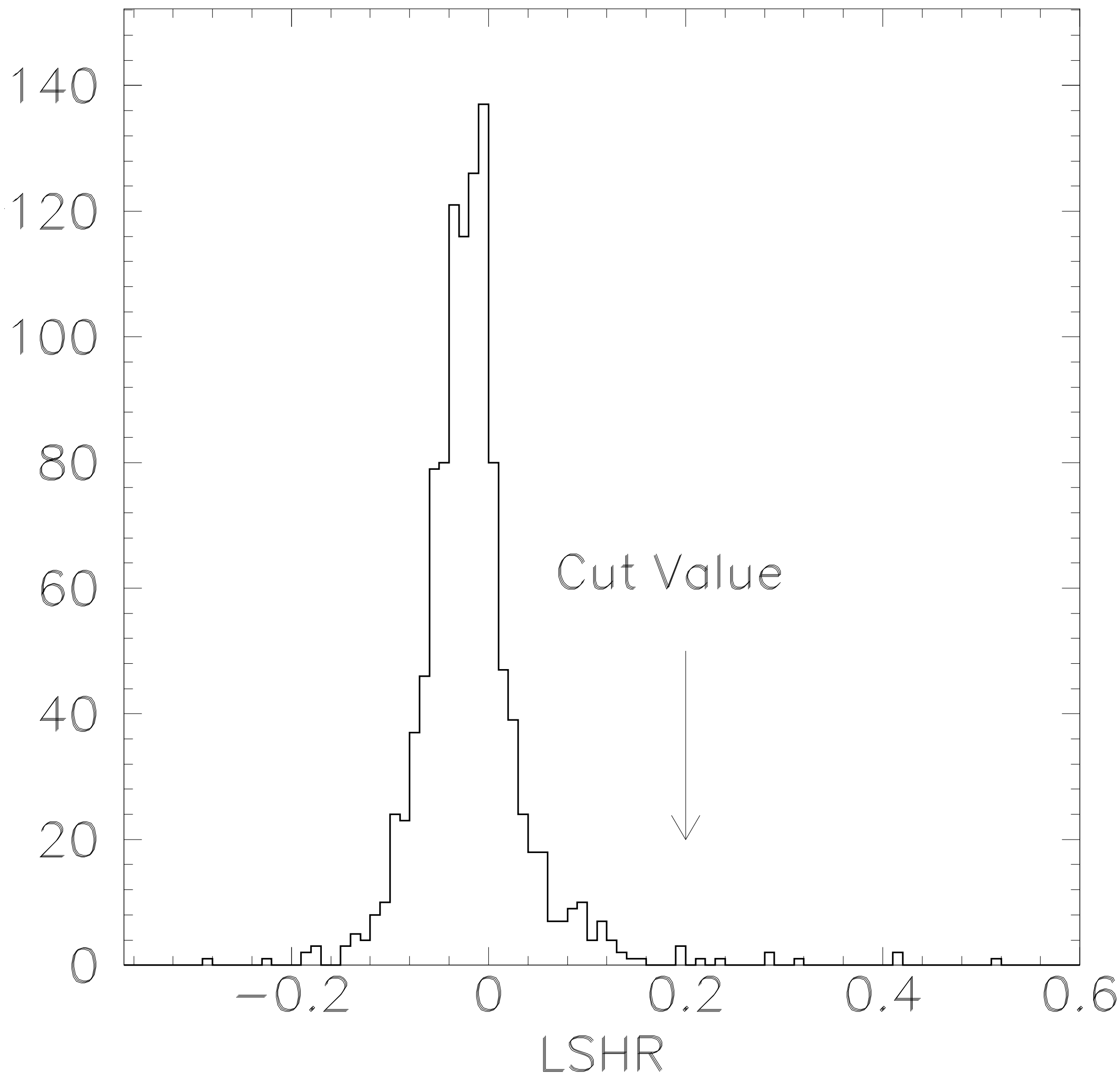

Figure 4: The distribution of the quantity $L_{\rm shr}$ for electrons from W decays. The small cone isolation trigger imposed a cut on this quantity at .2, as indicated.

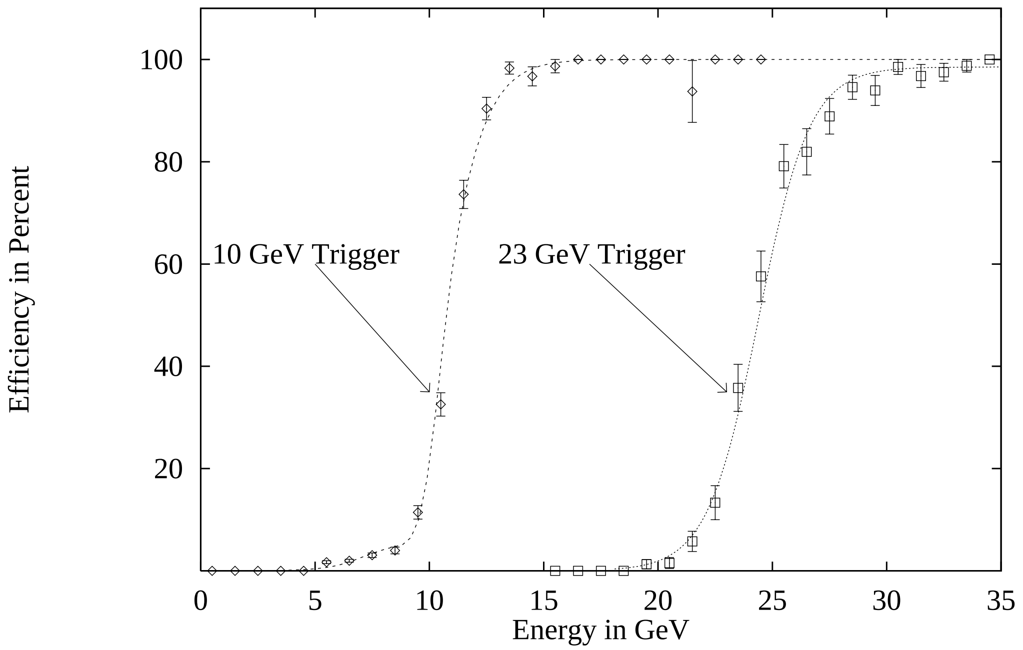

Figure 5: Trigger efficiencies for the 10 and 23 GeV photon triggers.

profile had $\tilde{\chi}^2$ larger than 20.

Only events that had no reconstructed tracks in the central tracking chamber pointing at any of the towers in the cluster were considered isolated photon candidates. A prompt photon is expected to convert in the beam pipe or vertex time projection chamber 3.5% of the time. The event fails the track cut in this case. The number of prompt photons was corrected for this loss.

Events were eliminated if there was a net imbalance of transverse energy, $S > 3.0$ where the quantity S is given by the expression:

$$S = \frac{\sqrt{(\sum E_x)^2 + (\sum E_y)^2}}{\sqrt{\sum \sqrt{{E_x}^2 + {E_y}^2}}}, \tag{5}$$

where the sums extend over all calorimeter towers in the detector, and E_x, E_y are the projections of the tower energies (in GeV). The events rejected by this cut were almost exclusively cosmic ray events that deposited energy only in the part of the detector that resulted in a trigger. An indication of how many of the events were consistent with actual photon events is given by comparing the pulse height found in the strip chamber for these events with the pulse height observed for events where there is transverse energy balance. Figure 8 shows this pulse height and contrasts the distribution of this quantity with that observed from uncut events. Since the bremsstrahlung photon from a cosmic ray muon will typically shower

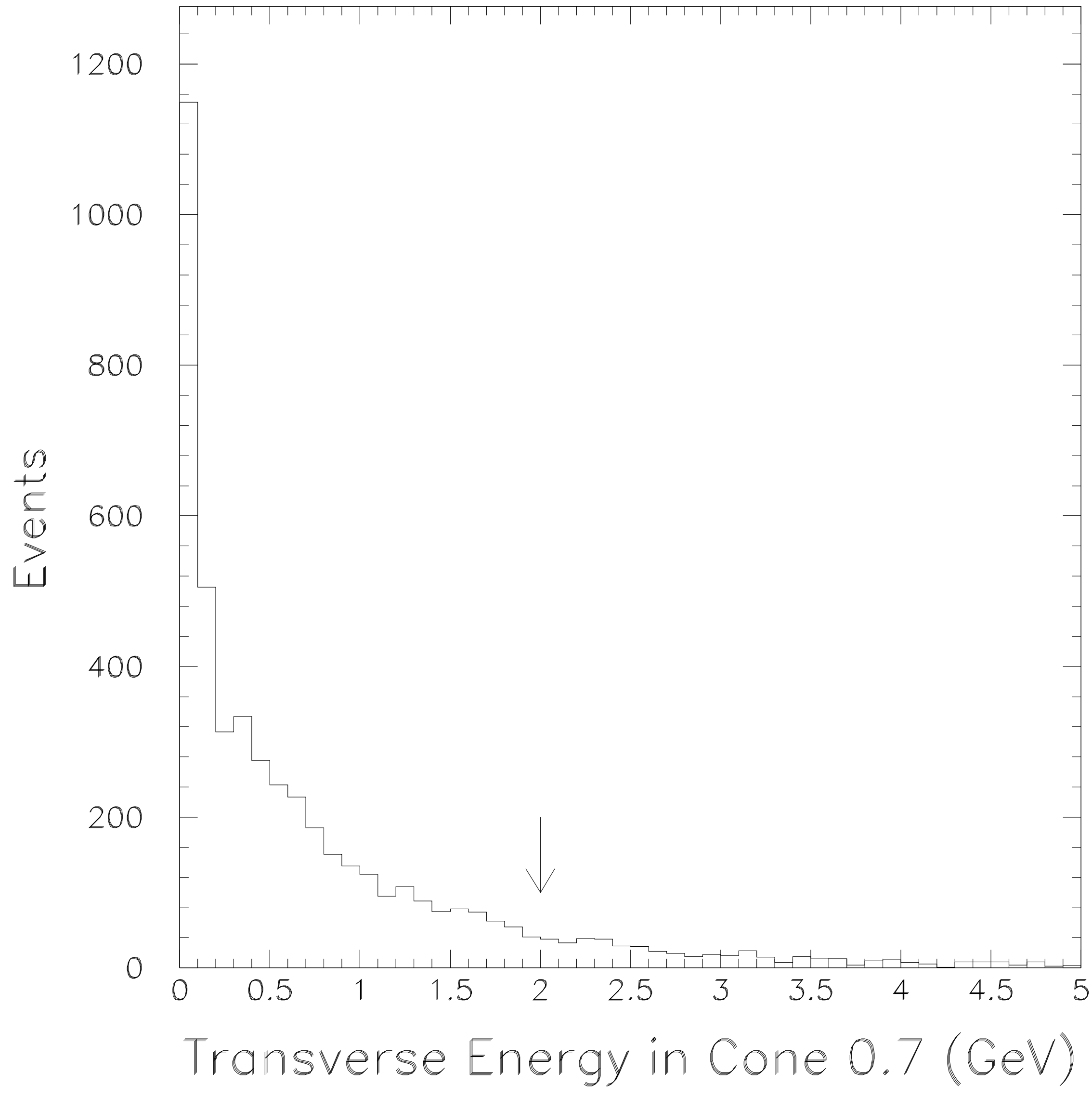

Figure 6: Transverse energy (E_T) in a randomly placed cone of radius 0.7 in a minimum bias event, representing the approximate underlying E_T expected for direct photon events. The arrow displays the 2 GeV cut value.

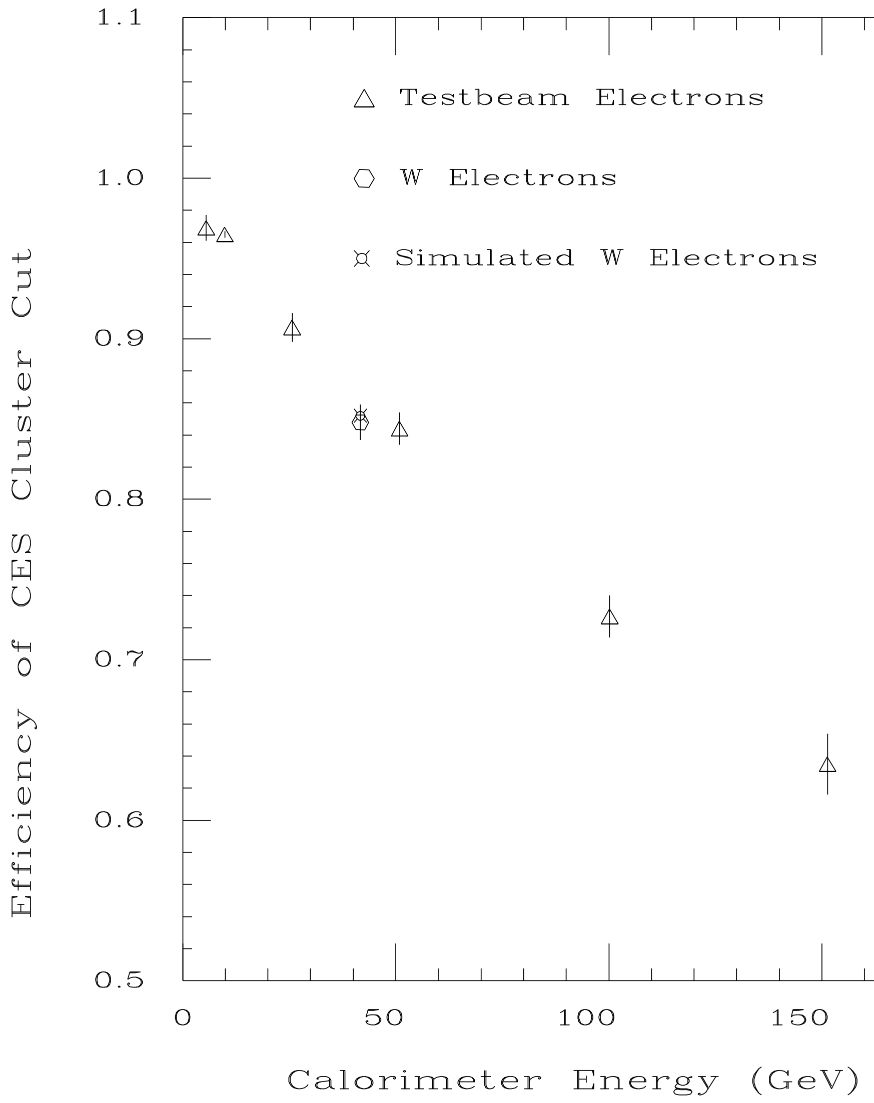

Figure 7: The efficiency of the 2nd CES cluster cut for different electron energies. The test beam electrons, and electrons from W decay (both measured and simulated) are shown.

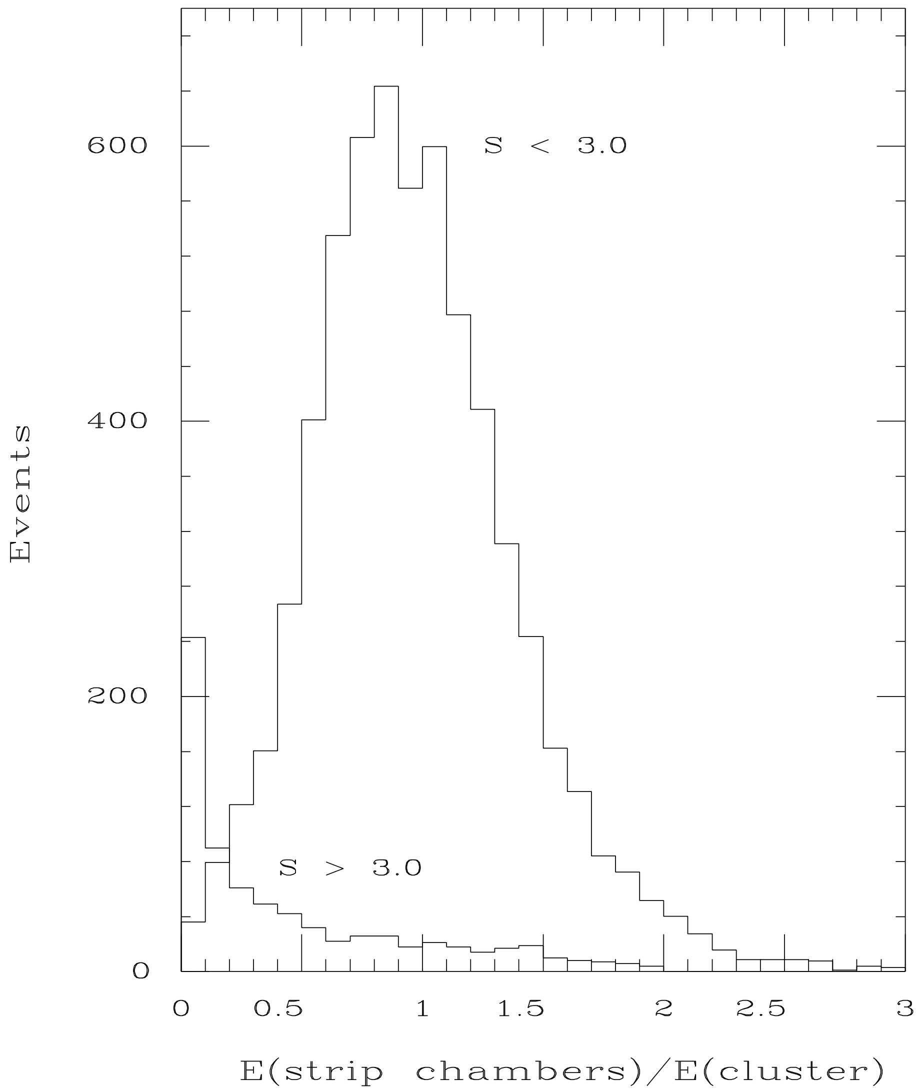

Figure 8: The strip chamber fractional energy response, E(strip chambers)/E(calorimeter), for two different cases: 1) Missing Transverse Energy Significance ($S > 3.0$) signifying a cosmic ray candidate, and 2) $S < 3.0$ signifying a prompt photon candidate.

more than 13 radiation lengths before the strip chambers (it is entering the detector from the outside), the majority of these events show very little strip chamber pulse height. The Fig. 8 distributions were used to estimate an upper limit on the event loss due to this cut.

When the *conversion method* is used to determine backgrounds, the event sample is limited to only events which have $\tilde{\chi}^2 < 8$. This imposes a small inefficiency but is desirable because it limits the class of background almost exclusively to π^0 decays. This decreases the uncertainty in the background evaluation and was loose enough to contribute very little to the systematic uncertainty for photon efficiency (5%).

Table 2 and table 3 summarize the event cuts applied to each sample, the number of events remaining, and give an estimate of the efficiency of each cut for prompt photons. Unless otherwise indicated, all the event samples discussed below were subjected to the cuts outlined above. There is a large reduction in the number of events from the initial sample to that in the final sample, for two reasons. The P_T cut is made to ensure a high trigger efficiency, at the loss of a number of events bunched near the threshold. In addition, the trigger had less stringent isolation cuts than the final sample; therefore the initial event sample is largely background that is eliminated by the offline cuts. After these cuts the P_T spectrum of the candidate events is shown in Fig. 9.

Table 2: Event Cuts, Counts and Efficiencies for the 10 GeV Trigger

Low P_T sample	52837	
$P_T > 14$ GeV number before all cuts	16004	
number after all cuts	1905	
CUT	NUMBER FAILING (ONLY THIS CUT)	PROMPT γ EFFICIENCY
$E_{\text{cone}} < 2$ GeV	2787	0.89
$\|x\|$ and $\|z\|$ fiducial cuts	474	0.64
extra strip/wire cluster	673	≈ 0.95
associated track	250	0.97
$S < 3.0$ (missing E_T)	20	> 0.99
$\|z_{\text{vertex}}\| < 50$ cm	250	0.88
Prompt γ efficiency for cuts listed above		0.46

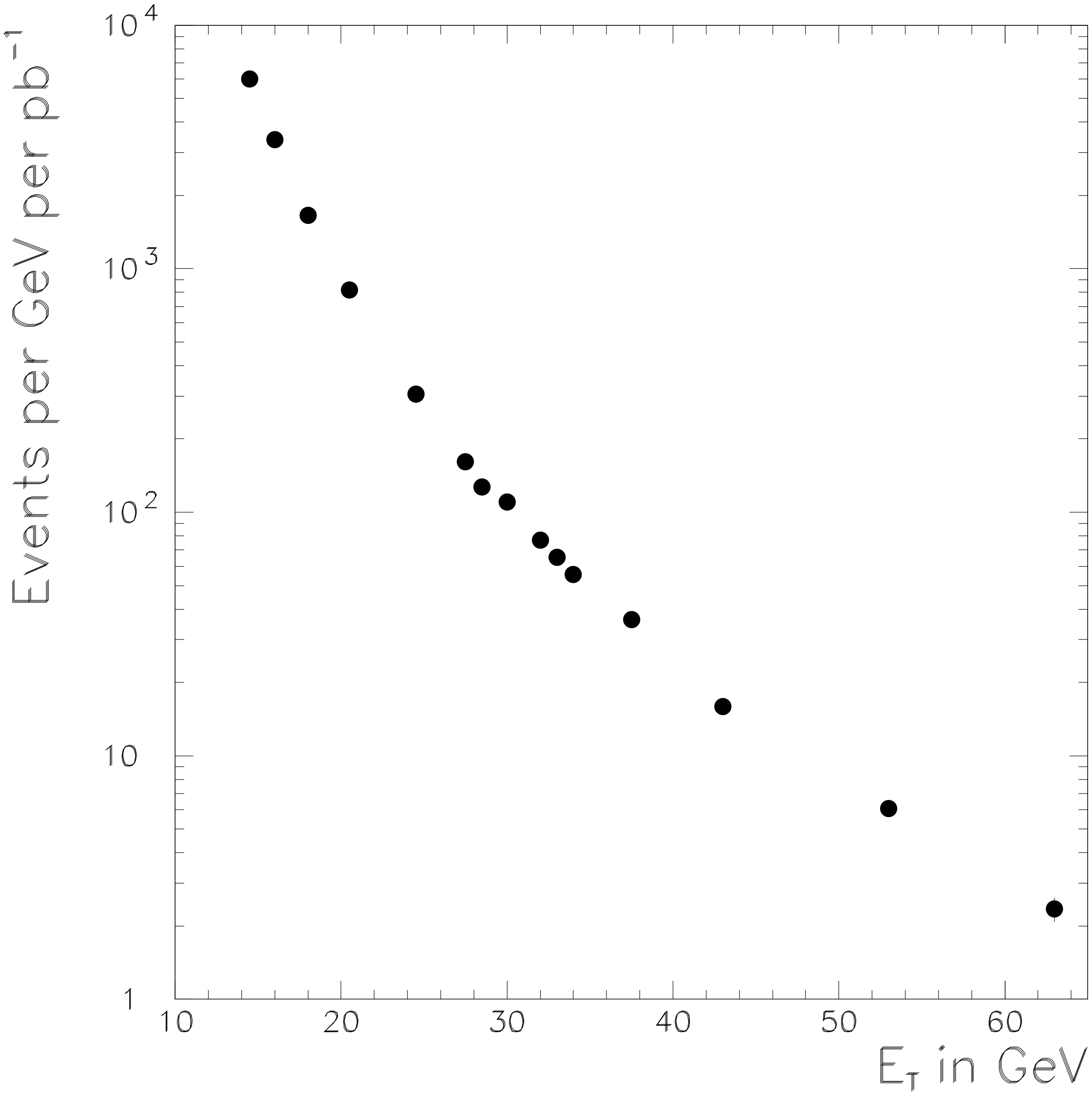

Figure 9: The P_T spectrum of the photon candidate events, after all event selection cuts.

Table 3: Event Cuts, Counts and Efficiencies for the 23 GeV Trigger

High P_T sample	91650	
$P_T > 27$ GeV number before all cuts	46295	
number after all cuts	2982	
CUT	NUMBER FAILING (ONLY THIS CUT)	PROMPT γ EFFICIENCY
$E_{\rm cone} < 2$ GeV	6927	0.89
$\lvert x\rvert$ and $\lvert z\rvert$ fiducial cuts	644	0.64
extra strip/wire cluster	407	≈ 0.9
associated track	502	0.97
$S < 3.0$ (missing E_T)	167	> 0.99
$\lvert z_{\rm vertex}\rvert < 50$ cm	283	0.88
Prompt γ efficiency for cuts listed above		0.43
$\widetilde{\chi}^2 < 8.0$ (conversion method sample)	1977	0.95

4 Electromagnetic Shower Simulation

Both methods for extracting the photon rate are sensitive to the expected efficiency of the background and signal. The conversion method depends on the amount of material and on the efficiency for detecting conversions. These do not require an extremely detailed simulation to model properly. Most of the information needed to properly evaluate the efficiencies can be obtained from data taken during the collider run. In contrast to this, the efficiencies for the profile method depend on the details of how the electromagnetic shower spreads out in the calorimeter and what fluctuations occur around the average shower profile. In order to evaluate these efficiencies a simulation based on actual shower data was developed.

An attempt to model the detector response using GEANT 3.14 [25] proved successful for gross features like the net ionization observed in the strip chambers versus incident electron energy. It did not, however, accurately predict the transverse shower profiles observed in test beam runs. This probably was due to the inability to model extremely low energy phenomenon (below 10KeV) in and near the sampling gas layer. GEANT was used to provide some guidance and intuition into the magnitude of some effects, but it could not be used as the basis for a detailed simulation.

At the simplest level the chamber samples electrons and positrons produced in the calorimeter as they pass through and ionize the gas layer. The shower statistics and thereby the scale of fluctuations is driven by the number of electrons plus positrons. This scale is measured by the net ionization observed in the chamber for showers of a given energy. The usual form for ionization or energy loss as a function of the depth, in radiation lengths, in the shower is given by [26]:

$$\frac{1}{E_0}\frac{dE}{dt} = b(bt_{\mathrm{CES}})^{bt_{\max}} e^{-bt_{\mathrm{CES}}}/\Gamma(bt_{\max}+1), \tag{6}$$

where E_0 is the energy of the electron or photon initiating the shower, b is a parameter dependent on the calorimeter material and weakly dependent on E_0, and t is the depth in radiation lengths. The values t_{CES} and $t_{\max}$ are the depth of the strip chamber and the shower maximum. The shower maximum depends on the initiating particle energy and type, as well as the calorimeter composition, as indicated in equation 7,

$$t_{\max} = \ln(E_0/E_c) - .5 + \delta, \tag{7}$$

where E_c is the critical energy of the material and δ is zero for a shower initiated by an electron and is an energy independent shift in shower maximum for photon initiated showers. In order to model the chamber response and the corresponding chamber statistics, a form of this type was used and the energy dependent parameter b was fit from test beam data. Figure 10 shows the average pulse height in the chamber as a function of electron energy for the runs used to find the parameter b along with the results predicted by the above formula.

The simulation used to calculate photon and background efficiencies was based on data taken in the Fermilab test beam. The response information used came from a number of runs done with a single central detector *wedge* in an electron enriched beam. The principal

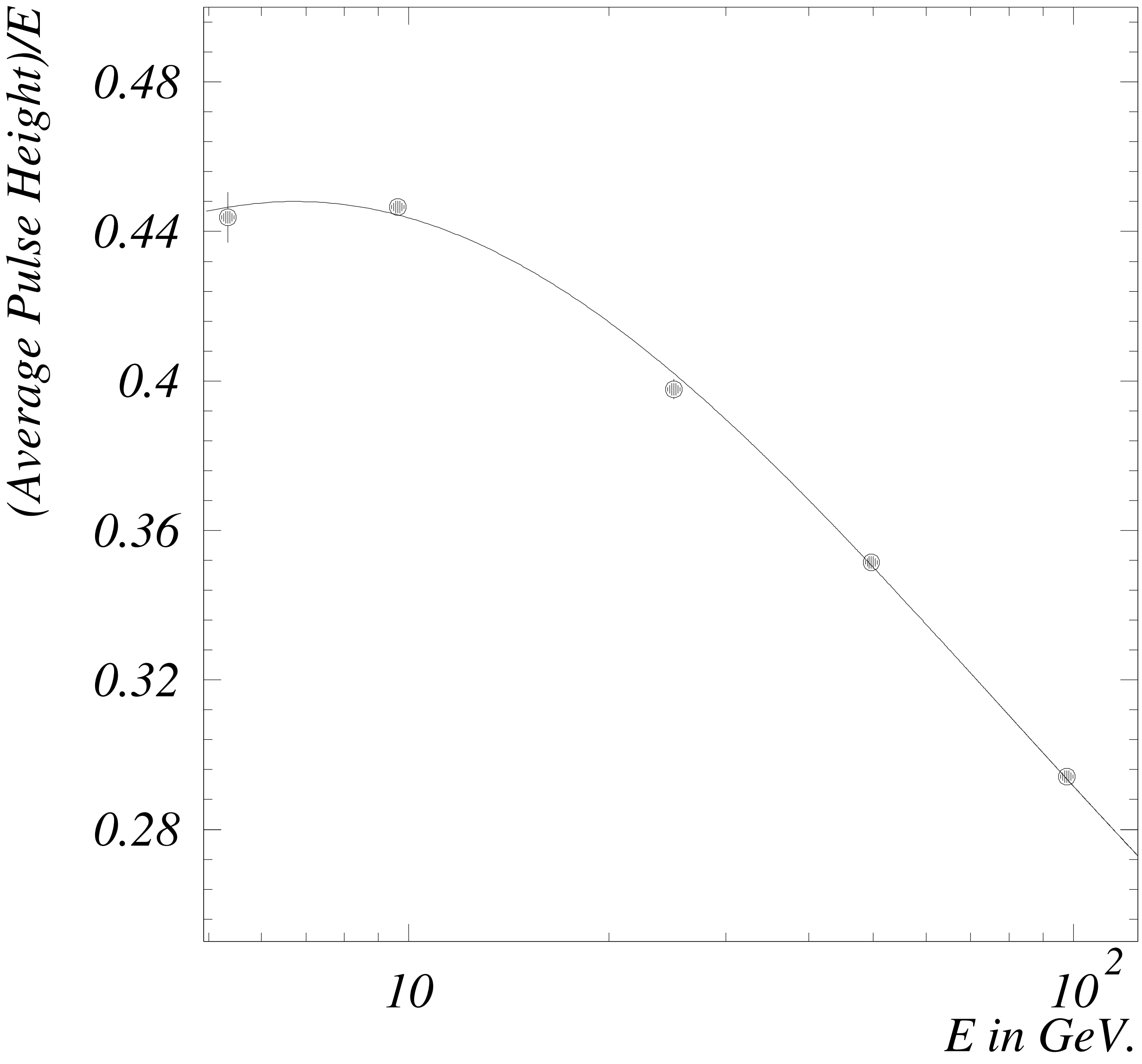

Figure 10: The average pulse height observed in the strip chamber divided by the beam energy. The data points are for test beam electrons and the solid line is the parameterization used in the simulation.

technique employed to simulate detector performance for the collider data was to use electron showers from this test beam running as the starting point for the more complicated collider events. This was done by scaling, translating, and superposing the strip chamber data from one or more test beam events.

Several small effects had to be incorporated to properly model the collider data. Test beam data was taken at 5, 10, 25, 50, 100 and 150 GeV. The energy dependence and difference between photons and electrons for the strip chamber was included by scaling the fluctuations from the values observed for a test beam electron to those expected for a simulated photon. In order to minimize any uncertainties caused by this procedure, test beam events were chosen from the test beam runs with energy immediately above and below the desired photon energy. Interpolation between test beam energies used a scaling formula for the fluctuations tuned to the overall energy dependence observed in the test beam runs.

Another effect was the difference expected for photon and electron showers. The strip chamber samples the shower at about six radiation lengths. Since the longitudinal development of photon and electron showers is slightly different (i.e. photon showers start later), the shower statistics and profile fluctuations are different. The profile method for determining the number of photons relies on an accurate accounting of the fluctuations around the mean profile. To model this difference, an adjustment to the fluctuations of the test beam electrons was made to match the expected fluctuations of an initiating photon in the simulation. This adjustment, while small, depended on the accuracy of a simple statistical model for the profile fluctuations. The scale of the fluctuations was taken as directly proportional to the square root of the average number of secondary electrons and positrons crossing the chamber for a given shower energy. This number in turn is proportional to the average pulse height observed in the chamber. The parameterization discussed above was used to characterize the energy dependence of the shower statistics. For photons the value δ in the above formula was taken to be 0.6. The residuals were scaled by the ratio of secondaries expected for photon initiated showers over electron initiated showers. The ratio of secondaries for photon showers over the corresponding number for electron showers, using the simple parameterization versus initiating particle energy, is compared to the ratio of secondaries calculated using a GEANT Monte Carlo simulation in Fig. 11.

The accuracy of the simulation was checked by comparing to data taken during the collider run. Electrons from W decay, photons from η decay, and π^0 mesons from $\rho^{\pm}$ decay were simulated and compared to data to confirm that the simulation was correct. These comparisons are discussed below.

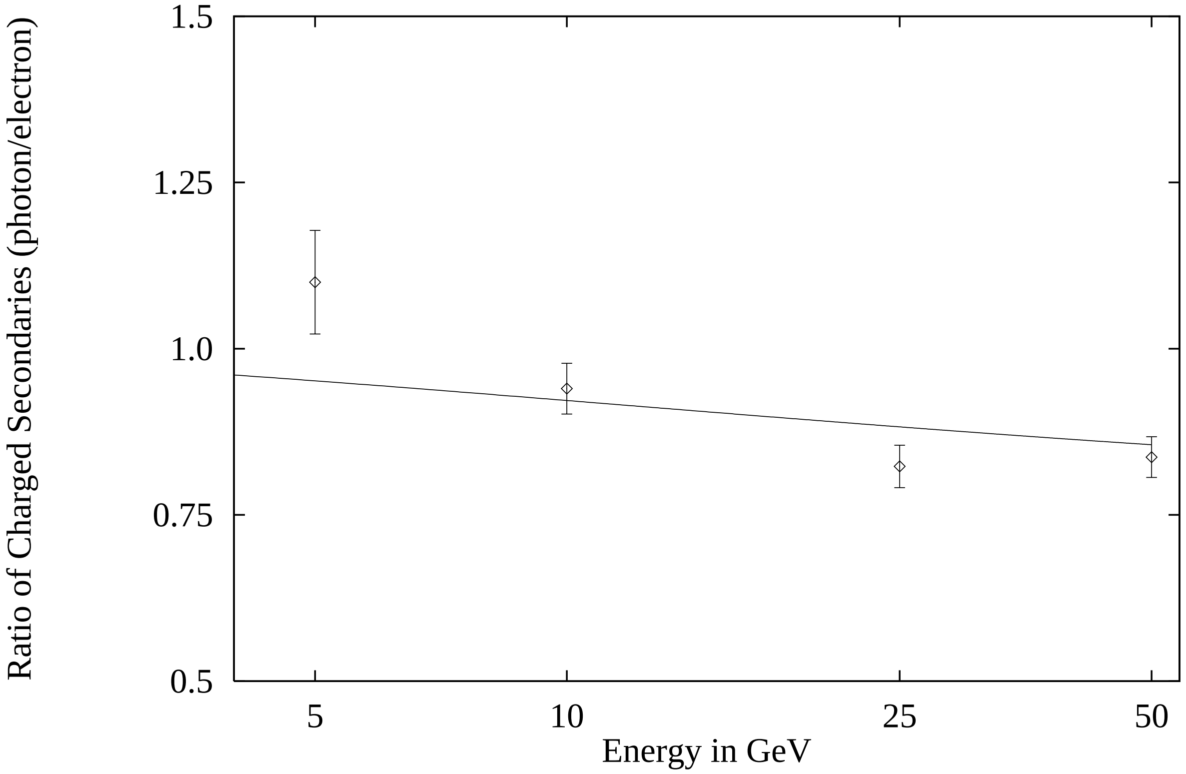

Figure 11: The number of electrons plus positrons impinging on the chamber sensitive volume for photon showers divided by the number for electron showers versus energy. The curve is from the parameterization used in the simulation. The data points are from a simulation using GEANT.

5 Profile Method Efficiencies and Systematic Uncertainties

5.1 Signal Efficiencies

The single photon efficiency (ϵ_γ) for passing the $\tilde{\chi}^2$ cut at 4 has been evaluated using the simulation. The efficiency shows a weak energy dependence but is approximately 80% throughout the range used to measure the cross section. The accuracy of the profile method depends critically on the ability to determine the efficiency for passing a cut in $\tilde{\chi}^2$ of both the single photons and the background. Two methods were available to check the validity of the values used. Electrons from the process W $\rightarrow e\nu$ provided a check on the test beam data used in the simulation. Decays of η mesons provided a sample of photons to check the remaining details of the simulation.

5.1.1 Cross Checks with W's and η's

Electrons from W decay were compared with the $\tilde{\chi}^2$ distribution expected based on the above simulation (see Fig. 12). The simulation of W decay electrons included radiation processes both in the decay and when the electrons passed through the inner tracking material[27]. The fraction of events that satisfy the requirement that $\tilde{\chi}^2 < 4$ is $0.785 \pm .012$ compared to the corresponding value for the simulated W electrons of $0.822 \pm .003$. The level of agreement between the simulation and the data indicates that for isolated electron showers at about 40 GeV, the test beam based simulation predicts the $\tilde{\chi}^2$ efficiency to the level of 5%. This level of agreement is what is expected from the evaluation of systematic uncertainties discussed later.

The $\tilde{\chi}^2$ distribution for photons is expected to be slightly different from that for electrons as outlined above. In order to check the simulation of photons, a sample of η mesons was identified in the data. They provided a source of two well separated photons. This sample came from the same event sample used for the single photon analysis, with only the cut on a single strip chamber cluster modified. For this analysis two clusters were required. A cut eliminating events with extra energy beyond the two clusters was applied. The η meson sample was obtained by requiring that the photons from the decay strike adjacent towers, thus ensuring that the energy of each photon is well measured. By using the locations of two photons reconstructed from the strip chamber information and the energy of the photons from the calorimeter information, the two photon mass can be reconstructed. A clear η mass peak is visible (see Fig. 13). In order to limit the effect of backgrounds to the η sample a side-band subtraction of the $\tilde{\chi}^2$ distribution was performed with the signal and side-band areas indicated in Fig. 13. Figure 14 compares the simulated distribution with the $\tilde{\chi}^2_S$ distribution from the η photons. The selection method, which requires that the photons strike adjacent towers, tends to result in well separated strip profiles but overlapping wire profiles. To ensure that this does not weaken the comparison, only the strip data was used for these plots.

The accuracy of the simulation used to obtain $\tilde{\chi}^2$ efficiencies is validated by W and η data

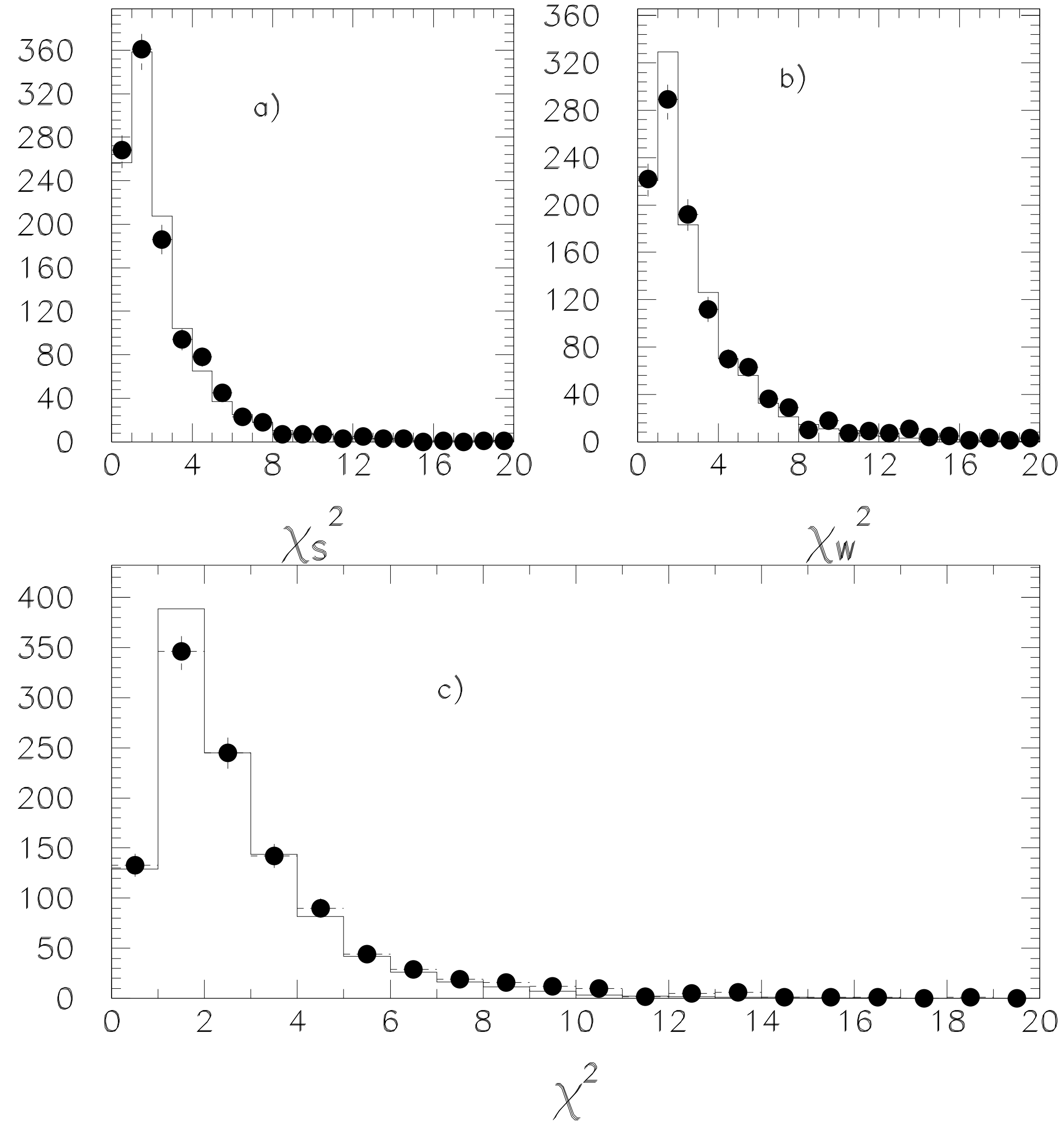

Figure 12: Comparison of electron $\tilde{\chi}^2$ from W decays(points) with a radiative W Monte Carlo plus detector simulation(histogram): a) strip view ($\tilde{\chi}^2_S$), b) wire view ($\tilde{\chi}^2_W$), c) Average of both views ($\tilde{\chi}^2$).

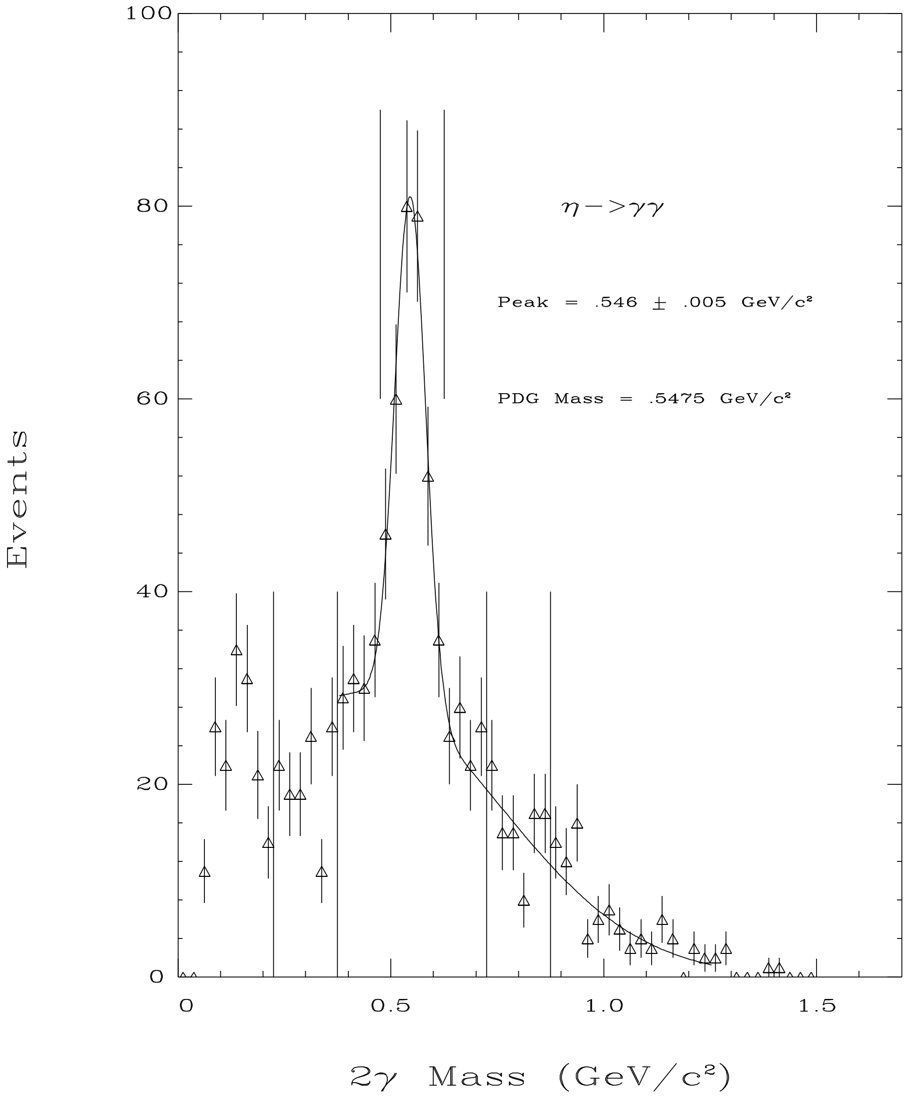

Figure 13: Two-photon mass distribution using 11 channel strip chamber clusters. The η meson peak is evident, while the π^0 peak is suppressed by the large clustering window. The lines indicate the peak and sideband regions.

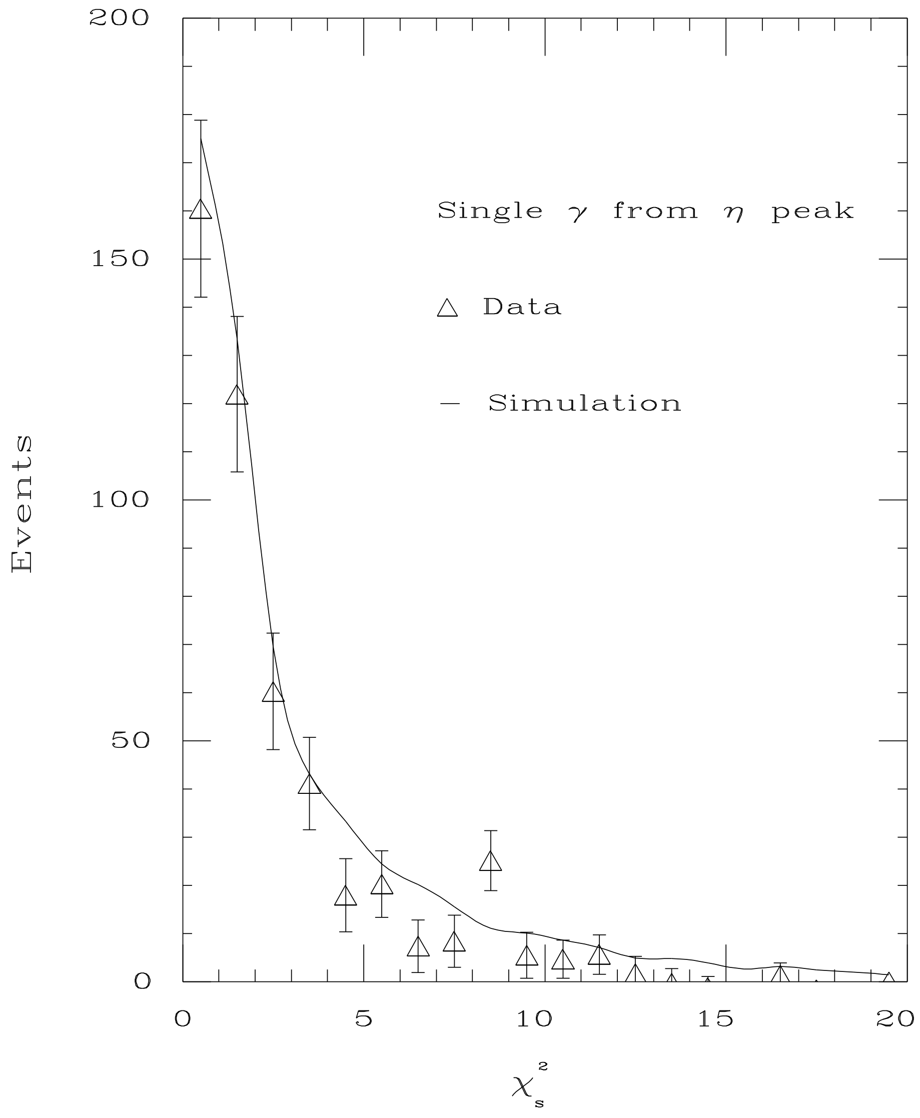

Figure 14: The $\widetilde{\chi_S}^2$ distribution (strip view) from the η mass peak is compared with simulated single $\eta \rightarrow \gamma\gamma$.

taken during the collider run. While the P_T distributions of these samples do not mimic that of the data (the W electrons have a typical P_T of 40 GeV and the η photons carry about 6 GeV), this does provide a measure of confidence that the tuning of the detector simulation is correct for both photons and electrons.

5.2 Background Efficiencies

5.2.1 Background Composition

Single π^0 mesons are the primary background to direct photons, but η mesons form a substantial additional contribution. Therefore it is necessary to know the relative production ratio in order to predict the $\tilde{\chi}^2$ distribution for the combined background. In order to measure the production ratio, small CES clusters (3 channels subtending 25 mrad) are used to separate the closely spaced photons from π^0s as well as ηs. The two CES clusters are required to be in the adjoining calorimeter towers to ensure a good energy and mass measurement. Multi-π^0 backgrounds are reduced by requiring the energy sum of extra CES clusters be less than 30% of the sum of the highest two. Misidentification of single photon showers as a π^0 at the tower boundary is reduced by requiring the two towers' energy asymmetry ($|E_1 - E_2|/(E_1 + E_2)$) to be less than 0.8. Figure 15 shows the resulting mass distribution, with the clear π^0 and η peaks. Also shown is the background fit (2 gaussians + polynomial), and the estimated distribution of single photons misidentified as π^0s. After a sideband background subtraction, and the proper acceptance correction, the resulting η/π^0 ratio is $1.02 \pm .15(\text{stat}) \pm .23(\text{sys})$. This ratio is then used to form the combined background $\tilde{\chi}^2$ distribution for π^0's and η's.

The process $K_S^0 \rightarrow \pi^0\pi^0$ also contributes slightly to the direct photon background, in particular, at the higher P_T region. For completeness this contribution was also added to our standard mix of simulated backgrounds. The production of K_S^0 has been measured by this experiment, during the 1987 collider run, using charged decay modes[28]. A value of K_S^0/π^0 of 0.4 was used in the simulation, based on this measurement.

The relative mix of single particle background is illustrated in the next two figures. Figure 16 shows the fraction of photons and background (having already passed the fiducial cuts) that also pass the "physics" cuts, namely, the cone isolation, no second CES cluster, and $\tilde{\chi}^2 < 20$. Figure 17 is the same plot for the background only, with the relevant production and branching ratios taken into account, demonstrating the dominance of single π^0's.

Due to the isolation cuts applied, the background due to multiple particle jets (i.e. 2 π^0) is expected to be small (comparable to or smaller than the K_S^0 contribution). Estimates of jets with 2 collimated π^0s were made based on the jet cross section P_T dependence and measured jet fragmentation distributions. These indicate that the multiple particle background is <5% of the other backgrounds. This estimate is corroborated by measurements of background conversions that will be discussed later. These events often have $\tilde{\chi}^2 > 20$ and are not included in the evaluation of ϵ, even if they pass all other cuts. The contribution of the multiple particle background is difficult to model accurately and has not been included in the standard mix of simulated backgrounds. The systematic uncertainty (based on the limits given above) is negligible compared to the other uncertainties.

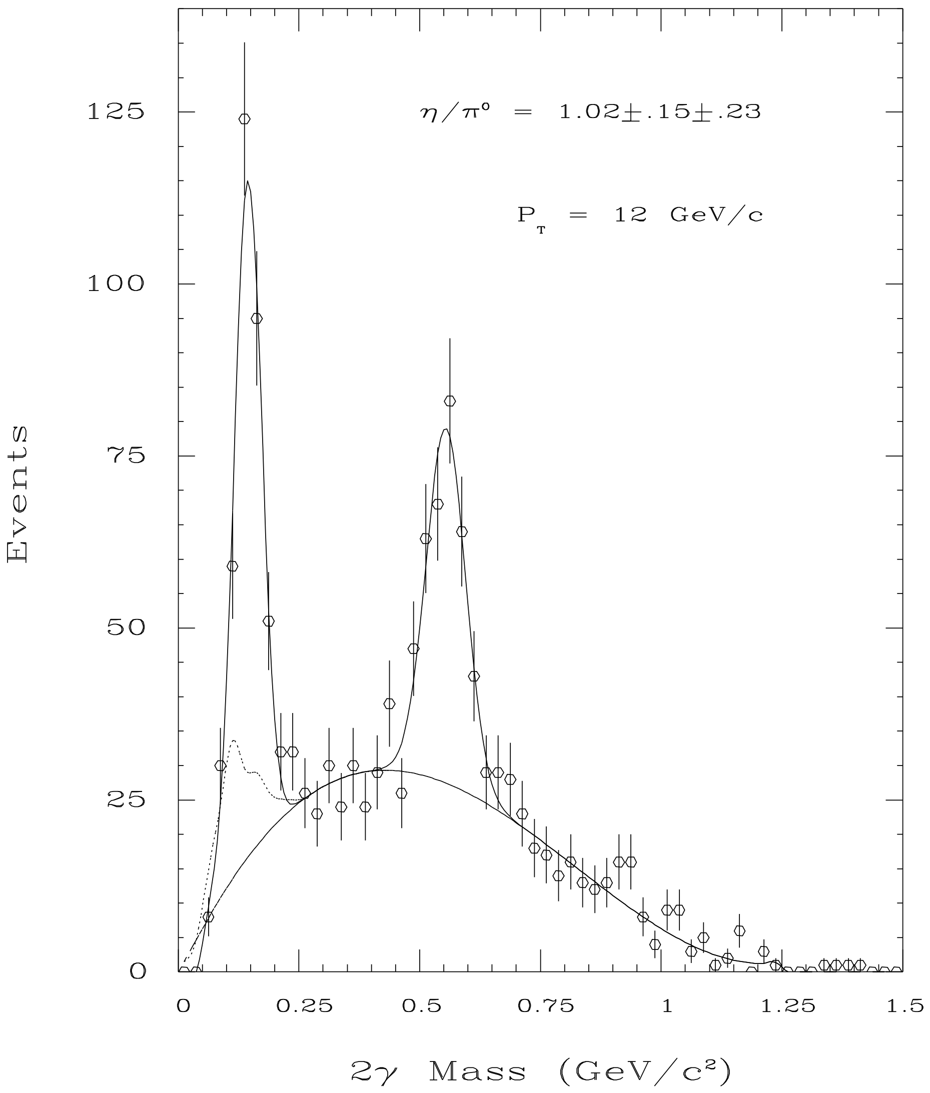

Figure 15: Two-photon mass distribution using 3 channel strip chamber clusters. The π^0 and η meson mass peaks are evident. Also shown is the estimated background distribution (smooth solid curve) and the sum of single photon contribution plus background (dots).

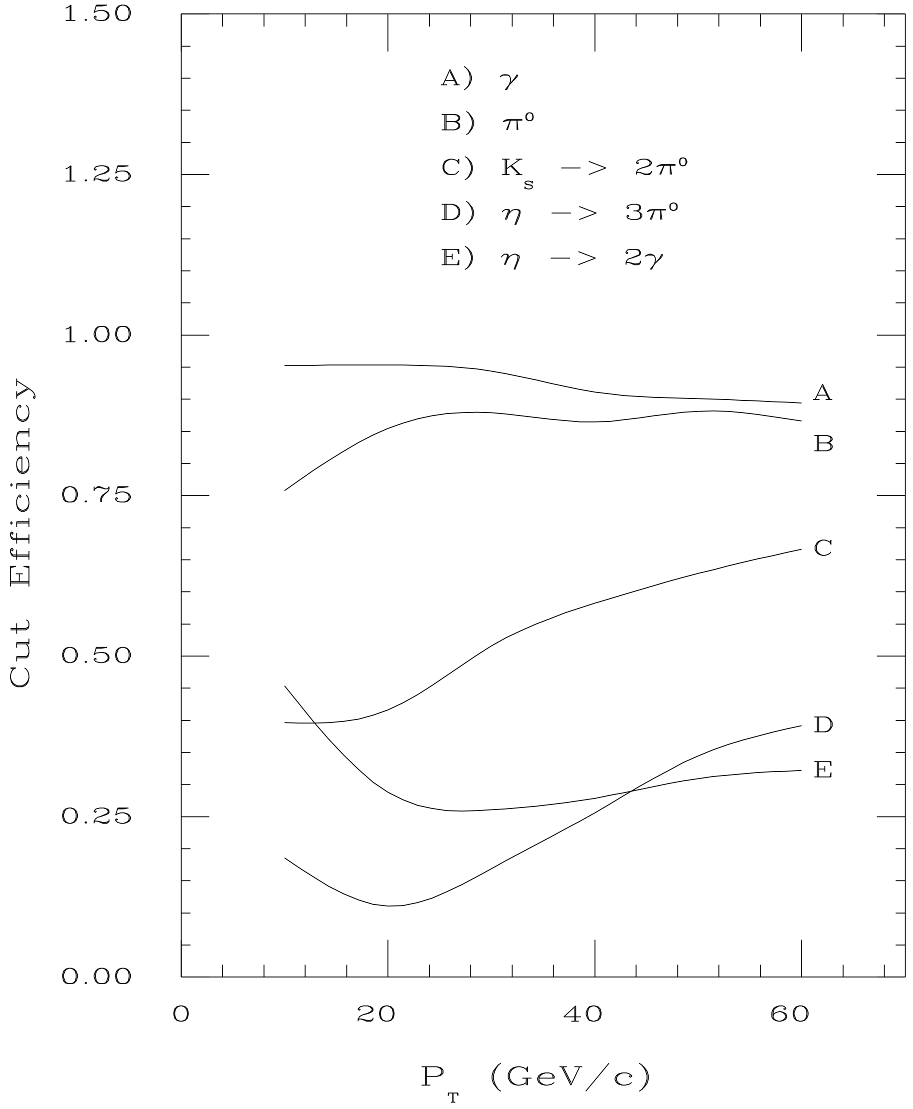

Figure 16: The fraction of simulated particles passing the CDF selection criteria.

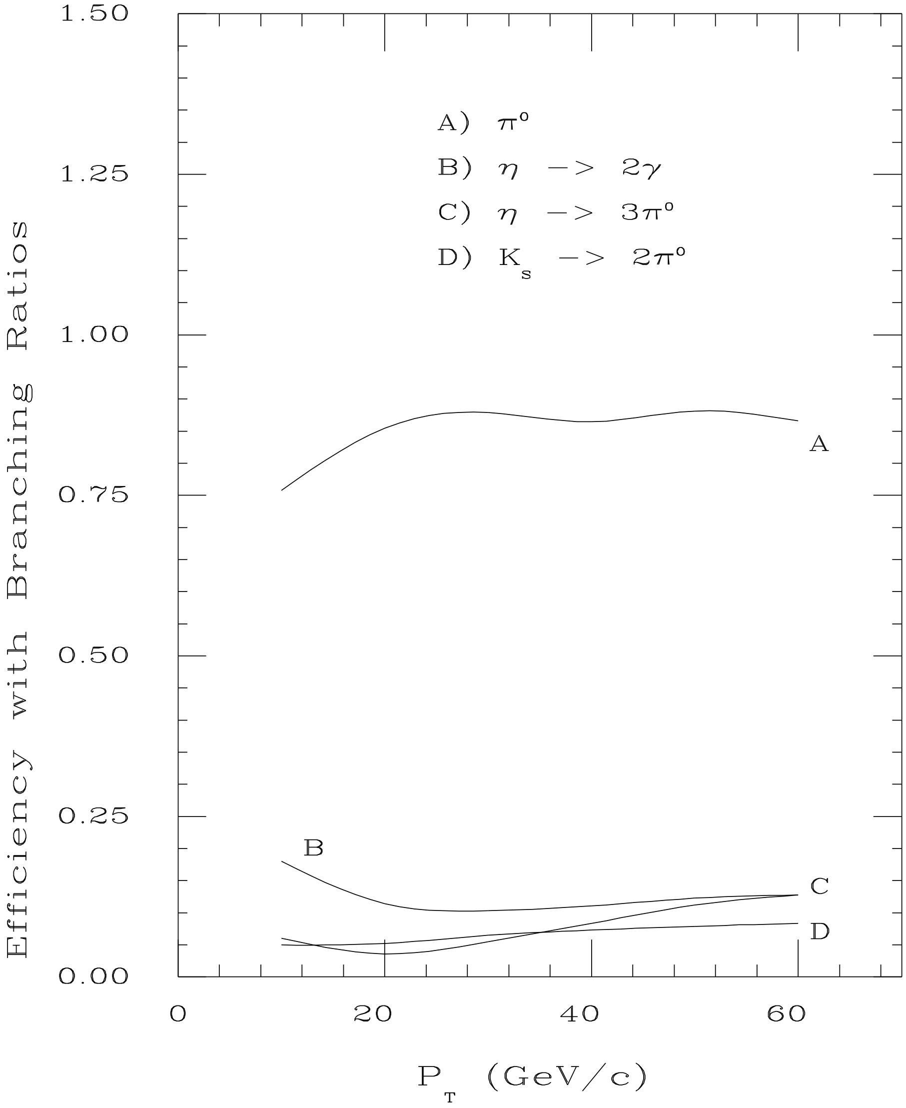

Figure 17: The fraction of simulated background passing the CDF selection criteria, taking into account the relevant production and branching ratios.

5.2.2 Combined Background Efficiencies

The efficiency for background events to pass a cut in $\tilde{\chi}^2$ at 4 was evaluated using the above production ratios and the simulation. All strip chamber and isolation cuts were applied to events before and after the cut, yielding an efficiency that tells how many events are in the sample compared to the number that have $\tilde{\chi}^2 < 4$. Figure 18 shows the P_T dependence of this efficiency. As the P_T rises the two photons from π^0 decay coalesce. The π^0 efficiency therefore rises at high P_T as the two showers overlap and become indistinguishable from a single shower. As the P_T decreases the likelihood of observing one photon from the η as a single isolated photon rises causing this efficiency to rise as P_T drops.

5.2.3 Cross Checks using $\rho^{\pm}$ Mesons

A $\rho^{\pm}$ sample was obtained by looking for events with a single charged track in association with a neutral electromagnetic shower. The mass distribution for the neutral plus the charged particle (the tracking chambers were used to reconstruct the charged particle momentum) is plotted in Fig. 19 for all such combinations in the final data sample. The charged track is required to have $P_T >.8$ GeV/c. A clear $\rho^{\pm}$ peak is observed. By fitting the mass peak excess above a smooth background in bins of $\tilde{\chi}^2$ for the neutral electromagnetic shower, a $\tilde{\chi}^2$ distribution has been constructed for π^0's from $\rho^{\pm}$ decays (see Fig. 20). The corresponding distribution for simulated $\rho^{\pm}$ decay π^0's is also plotted for comparison in Fig. 20.

5.3 Systematic Uncertainty on Efficiencies

The $\tilde{\chi}^2$ efficiencies of both the photons and the background are subject to a number of uncertainties. The cross checks mentioned above give us confidence that the method used to simulate the background and signal is reasonable, but a number of uncertainties remain and must be quantified to yield an estimate of the overall uncertainty in the number of prompt photons.

The efficiency for the background and signal are both sensitive to the same instrumental effects and are not discussed separately. A consequence of this is that the systematic uncertainties of both background and signal are highly correlated. A one standard deviation change upward in the photon efficiency due to a given source results in a corresponding one sigma upward change in the background efficiency. The uncertainties from three sources were included in the evaluation of systematics: the estimation of the difference between electrons and photons, the use of test beam showers taken under slightly different conditions than the collider running and the background composition.

An estimate of the uncertainty in the difference between photon and electron shower fluctuations was based on a variation of the shower parameterization. The P_T dependent range inferred from this variation is indicated in figures 21 and 22. Shower shape may be slightly different from electron to photon showers, an effect which has not been included. In order to evaluate how large an effect this might be we used electron test beam runs with different material in front of the calorimeter to see what the change in $\tilde{\chi}^2$ efficiency is when

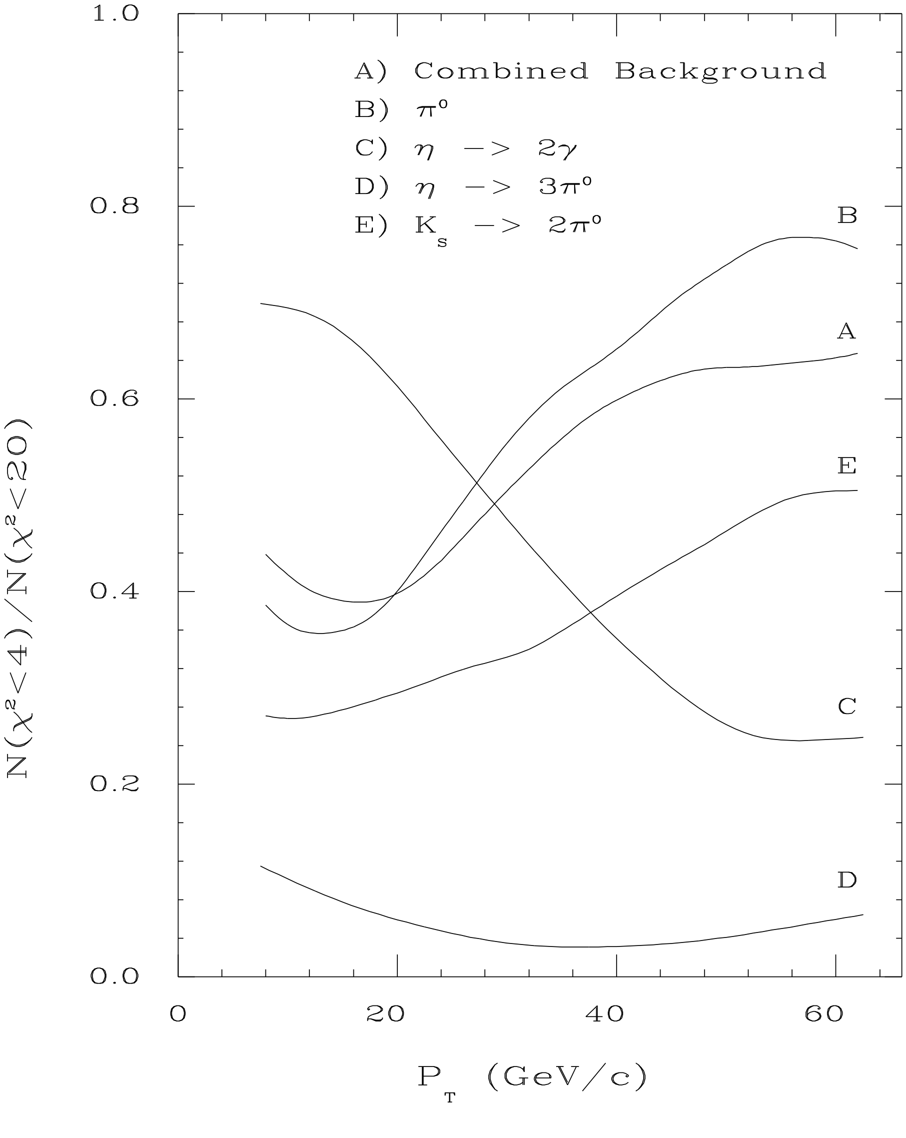

Figure 18: Efficiency for passing a cut in $\tilde{\chi}^2$ at 4 for the combined background and the individual particles that go into the background.

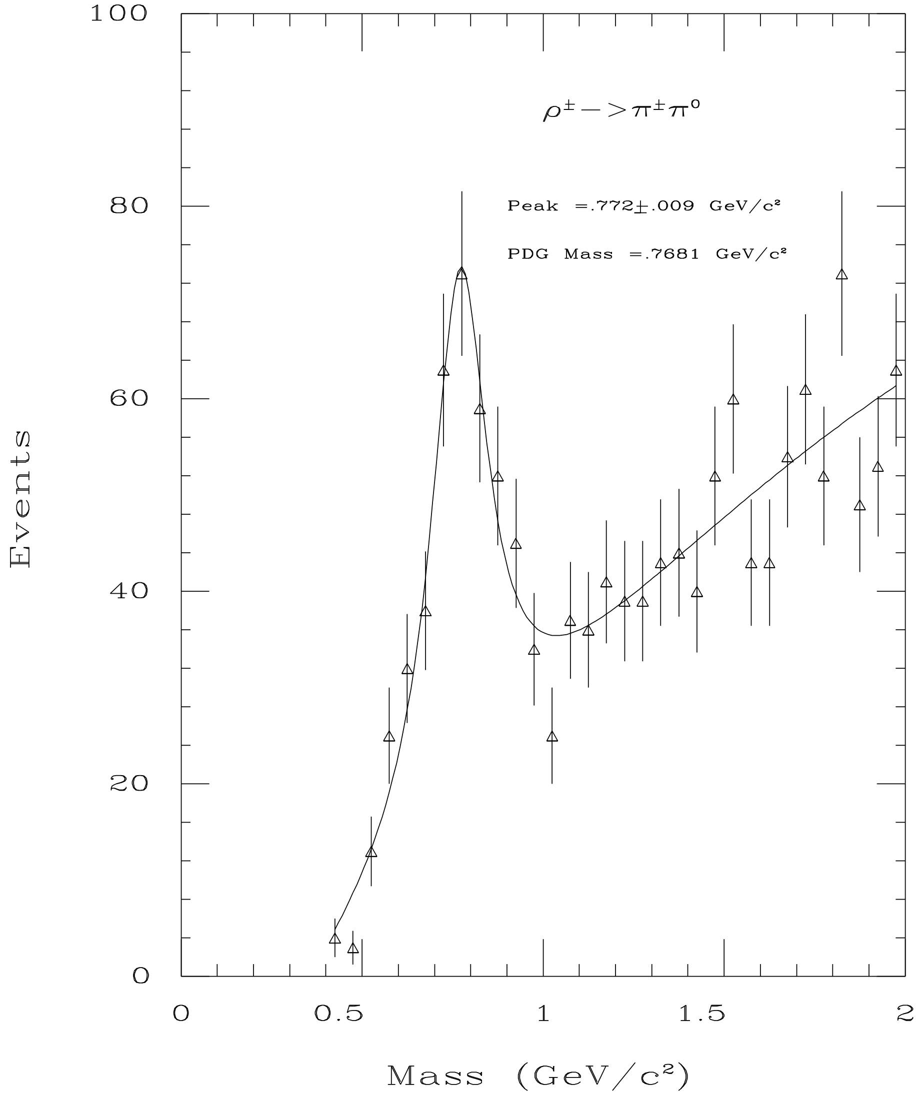

Figure 19: Photon candidate plus charged track mass distribution, showing the $\rho^{\pm}$ meson peak used as a cross check for the $\tilde{\chi}^2$ efficiency of π^0's.

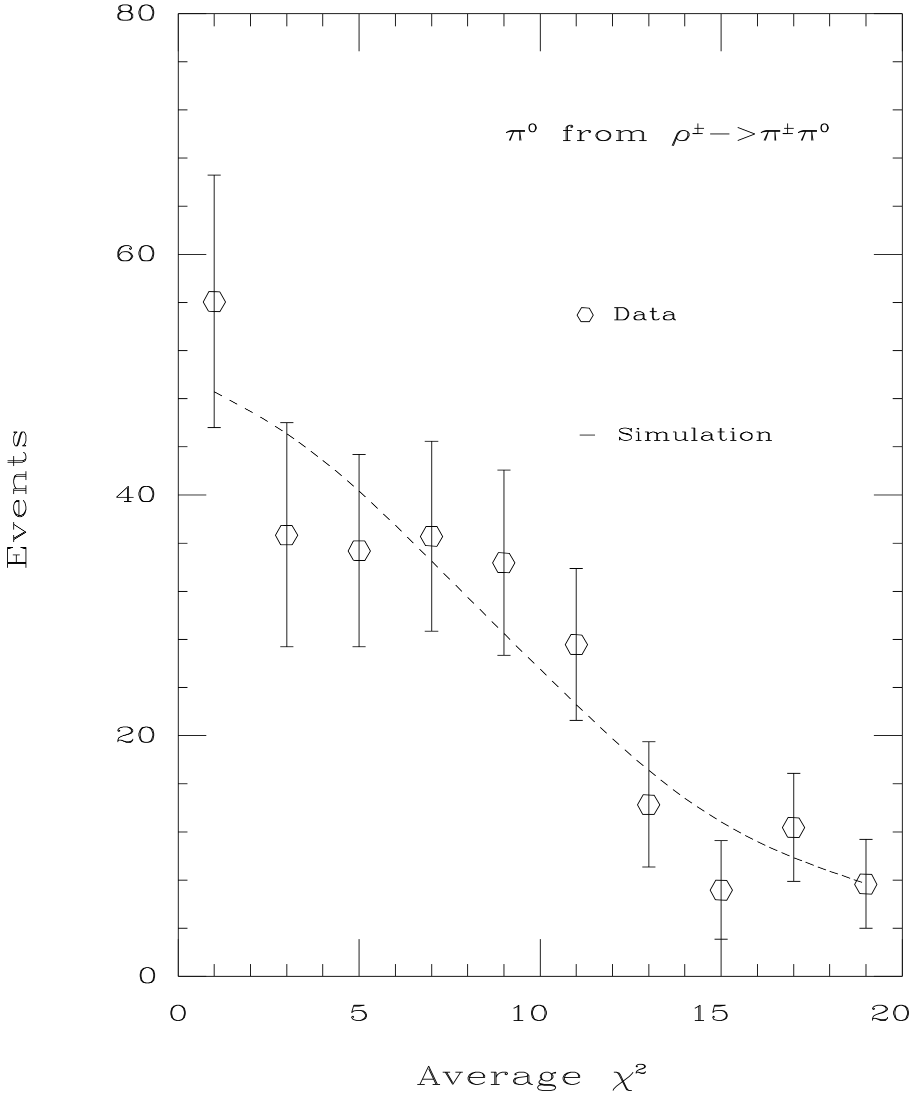

Figure 20: The $\tilde{\chi}^2$ distribution for the π^0's from the $\rho^\pm$ mass peak compared to simulated single π^0's.

the shower depth of the strip chambers is varied. An additional uncertainty was estimated from test beam runs with different chamber high voltage to cover the effects of saturation in the chamber. The level of each of these uncertainties and the dependence on P_T are indicated in figures 21 and 22.

The background efficiency is dependent on the particle ratios obtained from the data. The largest effect on the efficiency comes from the η/π^0 ratio. This has been taken to range from .75 to 1.3 and the range of resulting efficiency values is indicated in Fig. 22. The systematic uncertainty from this source is the smallest of the contributions discussed.

The overall efficiency for signal and background are shown in Fig. 23 along with the combined systematic uncertainty. Each of the above uncertainties has been added in quadrature. The signal and background errors are still fully correlated in this plot.

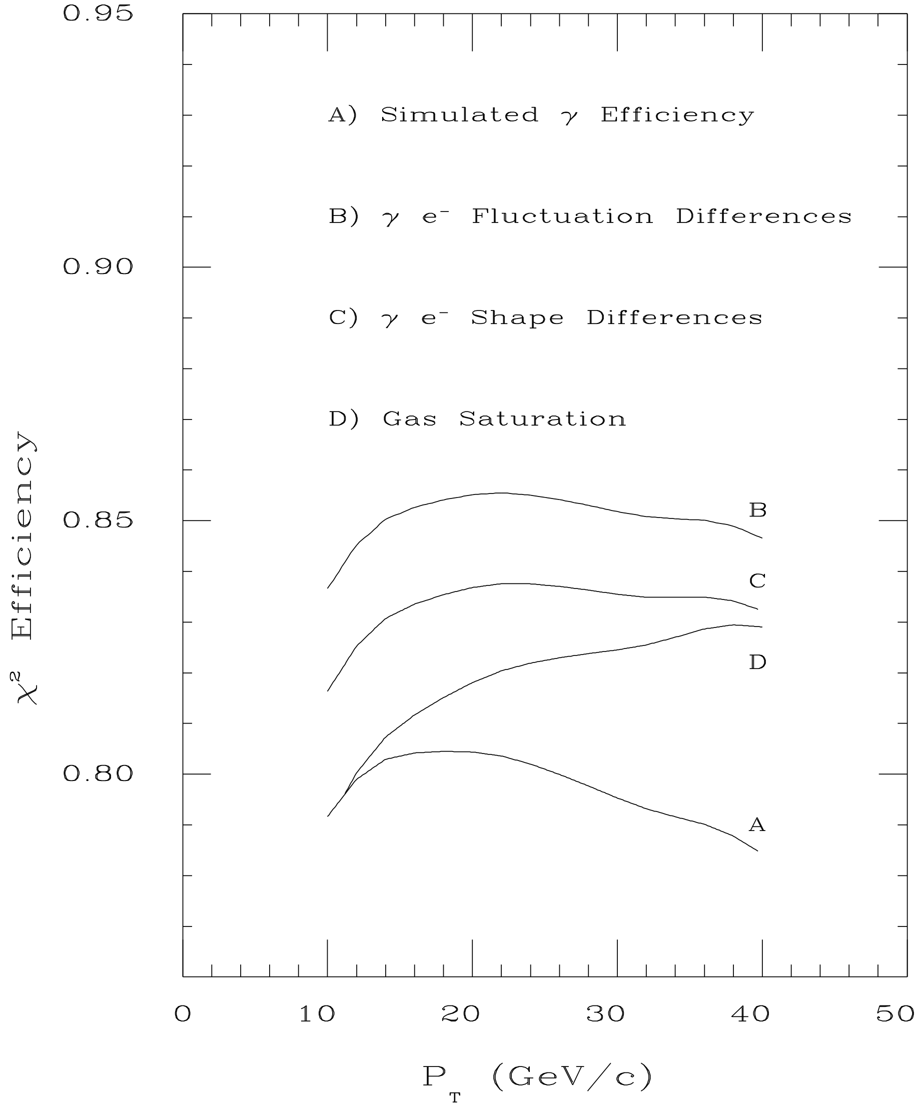

Figure 21: Simulated photon $\tilde{\chi}^2 < 4/\ \tilde{\chi}^2 < 20$ efficiencies. Also shown are the 1 σ upper systematic uncertainties due to shower fluctuations, shower shape, and gas saturation.

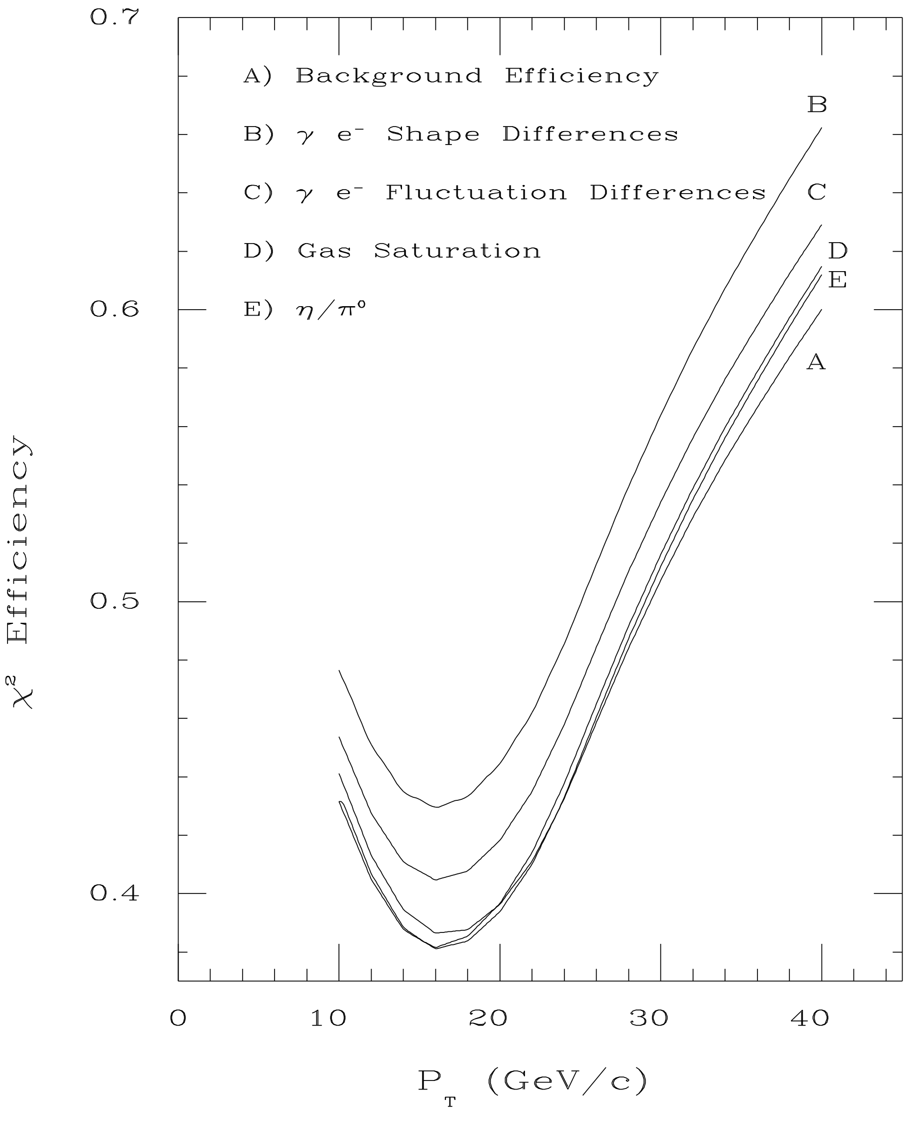

Figure 22: Simulated background $\tilde{\chi}^2$ efficiencies. Also shown are the 1 σ upper systematic uncertainties due to shower fluctuations, shower shape, gas saturation, and the η/π^0 ratio.

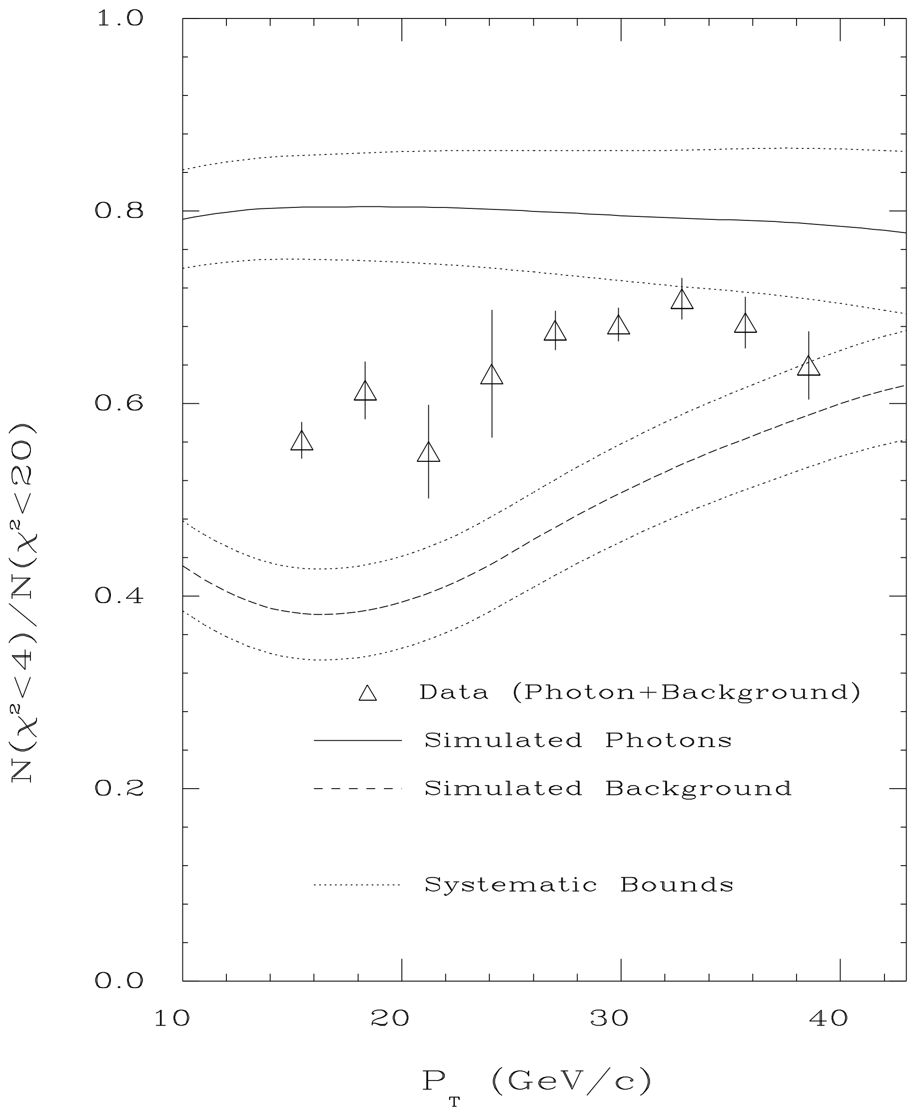

Figure 23: Signal and background $\tilde{\chi}^2$ efficiencies for the Profile Method. Also shown are the total systematic uncertainties on these efficiencies, and the measured efficiency of the data as a function of photon P_t.

6 Conversion Method Efficiencies and Systematic Uncertainties

In order to evaluate the cross section using the conversion method, the fraction of photon candidates with an observed photon conversion in the CDT was used. This fraction was used as ϵ in equation 1 to determine the relative contribution of single and multiple photon backgrounds in the sample. The probability that an event is observed to convert in the CDT depends on the number of radiation lengths available to convert photons, the CDT efficiency and the efficiency of cuts used in the analysis. Each of these contributions was measured using data taken during the collider run.

To improve position resolution and to minimize spurious hits, individual CDT hits were formed into clusters. Clustering was done using only the ϕ information. When there was a gap between hits of two or more tubes in ϕ, the hits were taken to be in separate clusters. The ϕ and z value of each cluster was the average over the hits. Clusters could consist of a single hit in the outermost layer but, to reduce background, single hits in the inner two layers were not considered. Due to the small amount of material in front of these layers single hits were more likely to be background than true conversions.

Events with charged tracks were used to check the overall performance of the CDT. CDT efficiency was studied with electrons from Z^o candidates, yielding an efficiency of 0.96 $\pm$0.02. Figure 24 shows the ϕ difference distribution for tracks with good agreement in z (2.5 cm or better) between the CTC and the CDT. The ϕ resolution is good because the tube size is small (0.0093 radian) and clustering futher improves the resolution. The z resolution is shown in Fig. 25 with tracks that have good agreement in ϕ (0.012 radian). Although the z resolution is about 2 cm, the distribution has a long tail caused by overlapping tracks.

To improve the signal to background ratio, clusters were required to be close to a calorimeter strip chamber cluster to qualify as a conversion and were considered associated with CTC tracks and ignored when $|\phi_{\rm track} - \phi_{\rm cdt}| < 0.01$ radian. We define the following notation for convenience, $\Delta\phi = \phi_{\rm wire} - \phi_{\rm cdt}$, $\Delta z = z_{\rm strip} - z_{\rm cdt}$, where *strip* and *wire* refers to the strip and wire measurement in the CES. The evaluation of $z_{\rm strip}$ included an interpolation to the radius of the CDT. In order to qualify as a conversion the CDT cluster had to satisfy a cut in both $|\Delta z|$ ($|\Delta z| \leq 10$ cm) and $|\Delta\phi|$ ($|\Delta\phi| \leq .07$). This window accepts almost all π^o decays and was large compared to the CDT z resolution. However, because of the long tails in the z resolution (Fig. 25), this cut reduced the efficiency of the Z^o sample to 0.73 $\pm$0.04. For the photon sample the efficiency was estimated by using the observed excess of events with clusters nearby in ϕ to the CES location for events that failed the cut in $|\Delta z|$, see Fig. 26. This excess comes from clusters that should have passed the $|\Delta z|$ cut but did not. The estimate of the CDT efficiency, including the cut in $|\Delta z|$, obtained in this way was 0.80 $\pm$0.05, which is consistent with the efficiency measured using the Z^o sample.

To correct for the contribution of accidentals in the CDT, the random hit contamination was estimated by counting the number of CDT clusters in windows 90^o away from the CES cluster in ϕ but at the same z. The random hit contribution was subtracted from the hit count to obtain the measured ϵ.

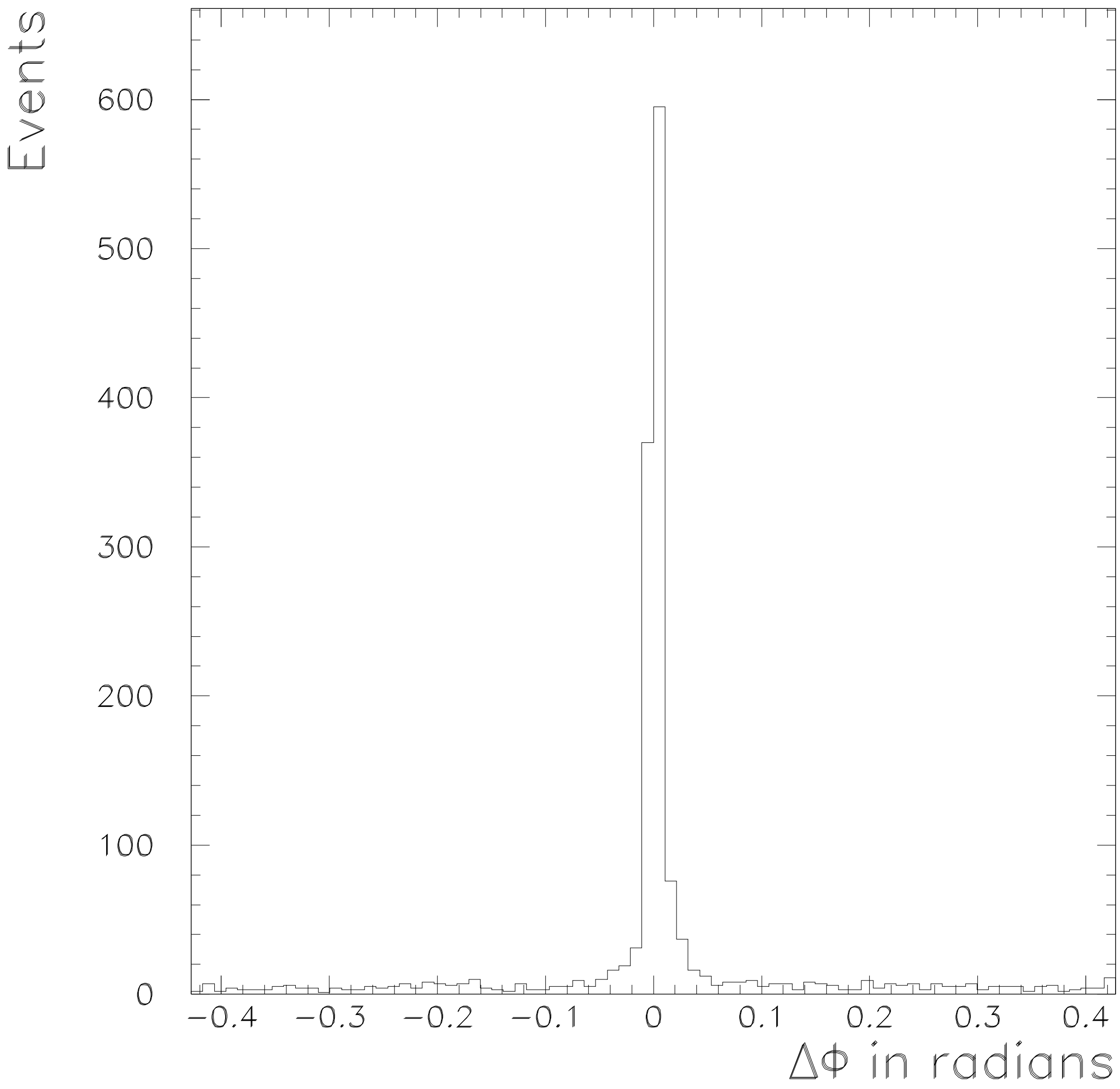

Figure 24: The difference between the ϕ observed in the CTC compared to the value observed in the CDT for tracks that satisfy a tight cut in $|\Delta z|$.

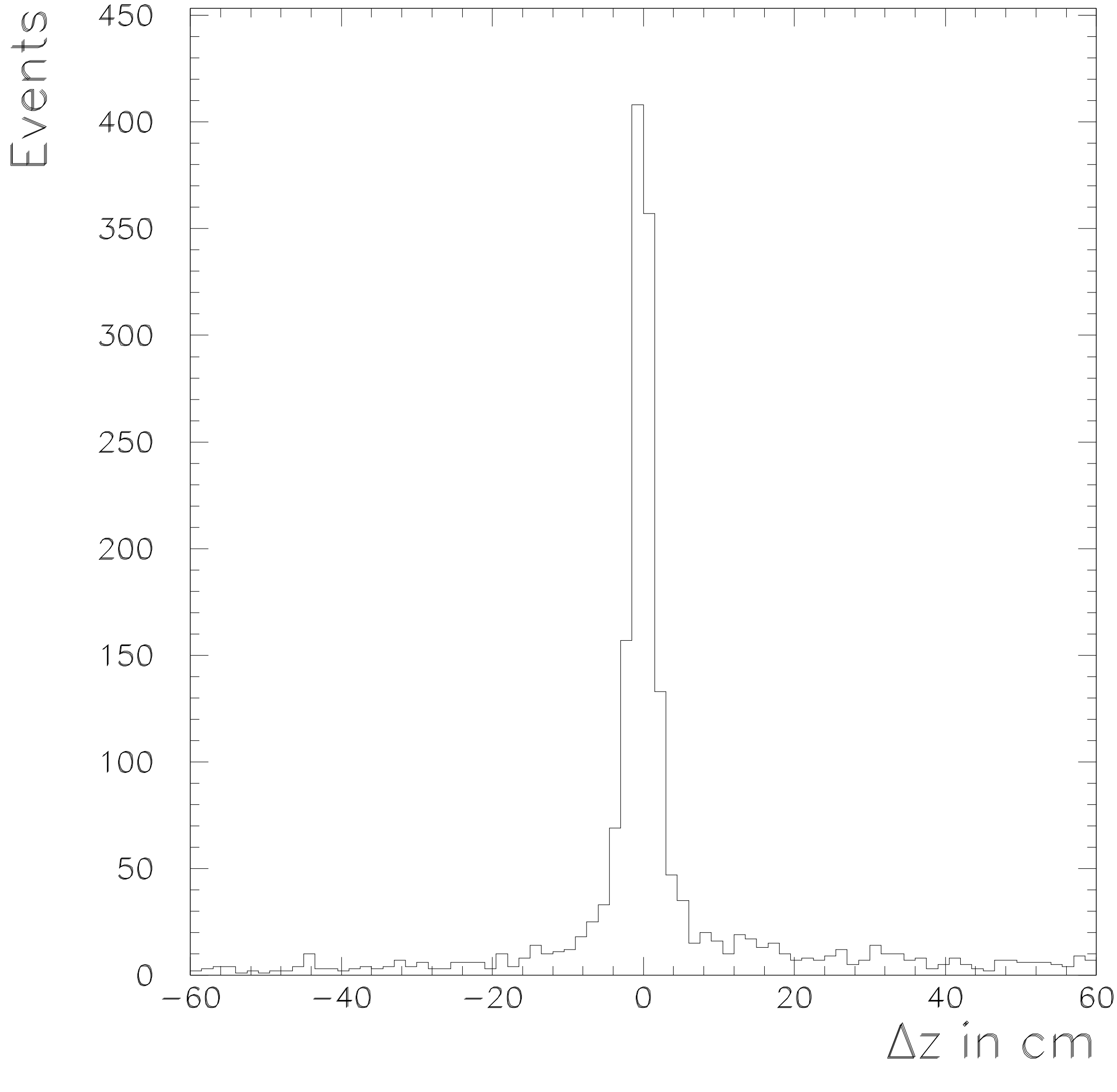

Figure 25: The difference between z observed in the CTC compared to the value observed in the CDT for tracks that satisfy a tight cut in $|\Delta\phi|$.

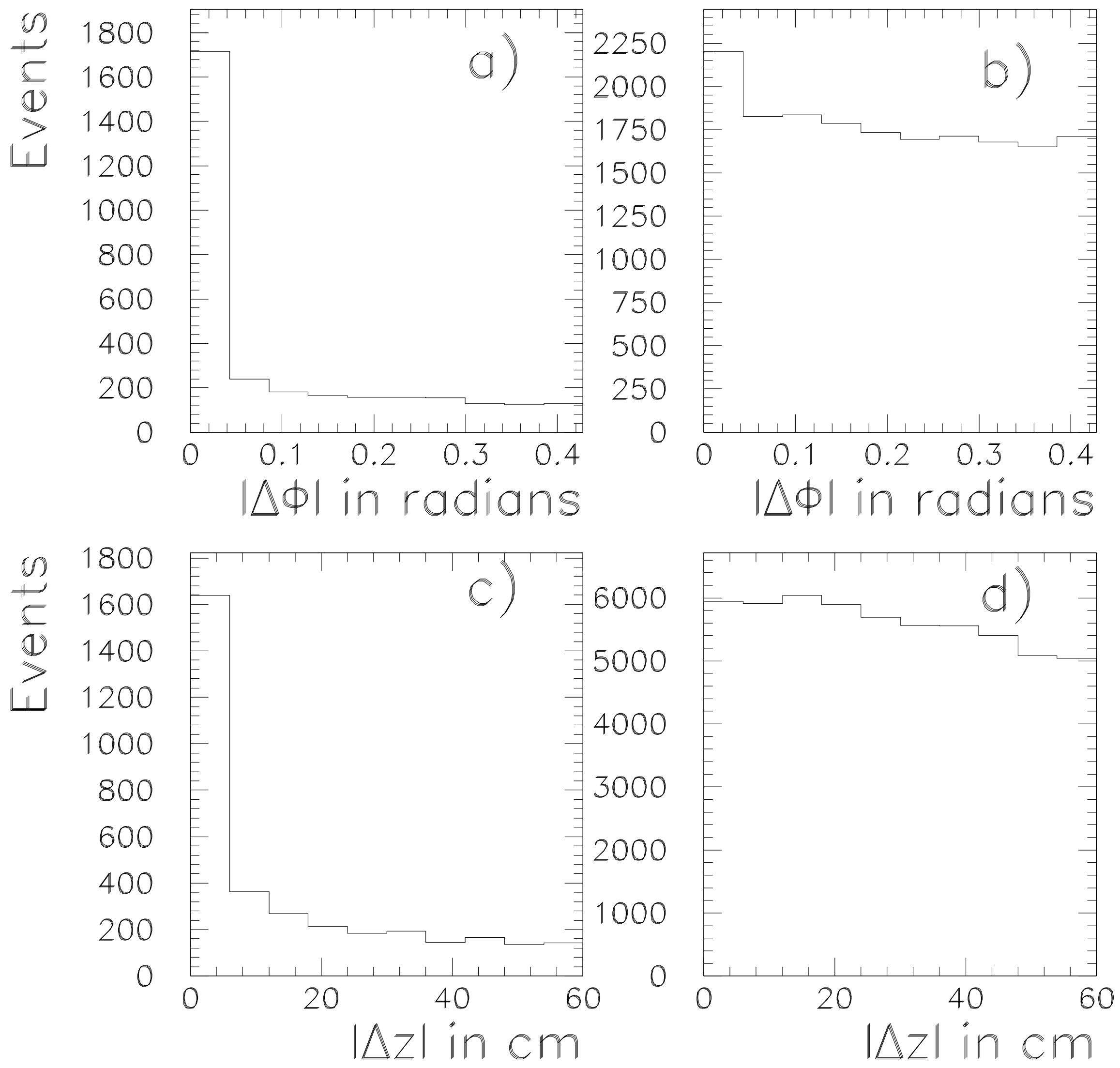

Figure 26: The effect of applying a cut in $|\Delta z|$ or $|\Delta\phi|$ is illustrated by these four plots. a) The distribution in $|\Delta\phi|$ for photon candidate events with $|\Delta z| \leq 2.5$ cm. b) The distribution in $|\Delta\phi|$ for photon candidate events with $|\Delta z| \geq 2.5$ cm. Note the excess of events at low $|\Delta\phi|$. c) The distribution in Δz for photon candidates with $|\Delta\phi| \leq 0.07$ radians. d) The distribution in Δz for photon candidates with $|\Delta\phi| \geq 0.07$ radians. Note that this distribution does not show the same excess as in b.

The conversion method depends on an accurate determination of the number of effective radiation lengths that photons traverse. This value was available from the known composition of the detector, but was checked and more accurately determined by using data from beam-beam collisions. A sample of events with a known fraction of single photons and π^0's was used. The conversion rate in this sample combined with the limits on the photon to π^0 fraction yields an estimate of the number of radiation lengths in front of the CDT. A sample of events which had low energy showers in the calorimeter (9 GeV/c $< P_T <$ 11 GeV/c) and appeared as single showers in the calorimeter strip chamber (i.e. had $\tilde{\chi}^2 < 4$) were selected. This sample was composed of π^0's and prompt photons almost exclusively. For the π^0 events a conversion might occur equally likely for either of the two photons from the decay. Some fraction of the time we expect the shower observed in the calorimeter chamber to be dominated by the non-converting photon, leading to a difference in the conversion position compared to the shower position in the strip chamber. Figure 27 shows the difference in azimuth observed between the CDT conversion and the calorimeter shower. A shoulder in the distribution is visible resulting from π^0 decays where the CDT conversion is not produced by the same photon that dominates the calorimeter shower. There is no mechanism by which such an event excess would arise from a single photon, so the size of this shoulder indicates the level of the π^0 signal. The peak around 0 is due to both single photons and π^0's; the contribution of π^0's to this peak must be at least equal to their contribution to the shoulder. By attributing the excess in the region around zero of this plot to prompt photons or π^0 decays (the latter corresponding to the assumption that there are no prompt photons in the sample) the contribution of one and two photon events can be bracketed. By using the observed conversion rate plus these two extreme assumptions, the single photon conversion rate is evaluated as $P_\gamma = 0.129 \pm 0.023$. This is very close to the expected value of 0.133 from an accounting of the material in front of and including the CDT tubes themselves.

Provided CDT clusters come from conversions, the probability that a photon yields an observed cluster is independent of energy and can be used to determine the photon and multi-photon rates using equation 1. In order to check that hits in the CDT originate from conversions and not from backscattering particles from the calorimeter, the rate excess caused by structural ribs in the CTC outer case was used. While the material in the CDT and CTC outer case is not that well known, eight reinforcing ribs of 1.59 cm wide aluminum straps break the azimuthal uniformity of the material. The enhancement of the conversion rate at these ribs can be seen in Fig. 28. The enhancement is consistent with the expected additional material. This agreement indicates that backscatter from the calorimeter is not a major contributor to the CDT hit rate. In addition a GEANT simulation was performed to check that backscatter did not contribute significantly to the CDT hit rate. This study indicated that the backscatter contribution to the hit rate is less than 1.3% .

In summary the probability that a photon produces an observed CDT conversion (ϵ_γ) is 0.095 $\pm$0.017. This includes the expected single photon conversion rate using the estimated amount of material ($\sim$18% of a radiation length at θ=90^o), the loss due to overall CDT inefficiency ($\sim$4%) and the Δz cut inefficiency ($\sim$ 27%).

A Monte Carlo study was done to estimate the expected hit rate for backgrounds, ϵ_b.

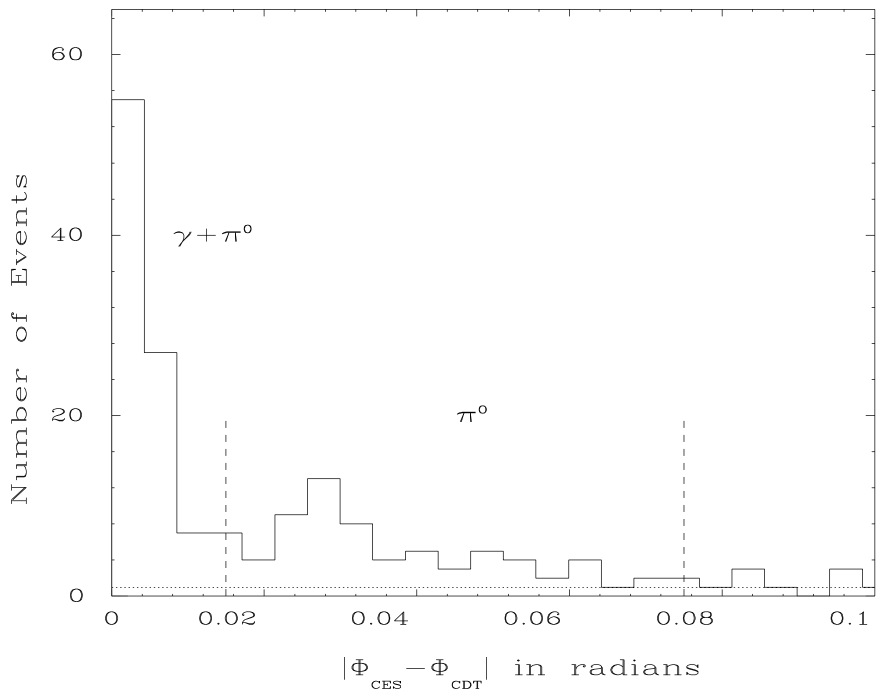

Figure 27: Difference in azimuth position of the strip chamber cluster and the CDT cluster for 9-11 GeV P_T photon candidates after a $\widetilde{\chi^2} < 4$ cut. The $\tilde{\chi}^2$cut selects asymmetric decays of the π^0, which are seen as an excess near .028 radians.

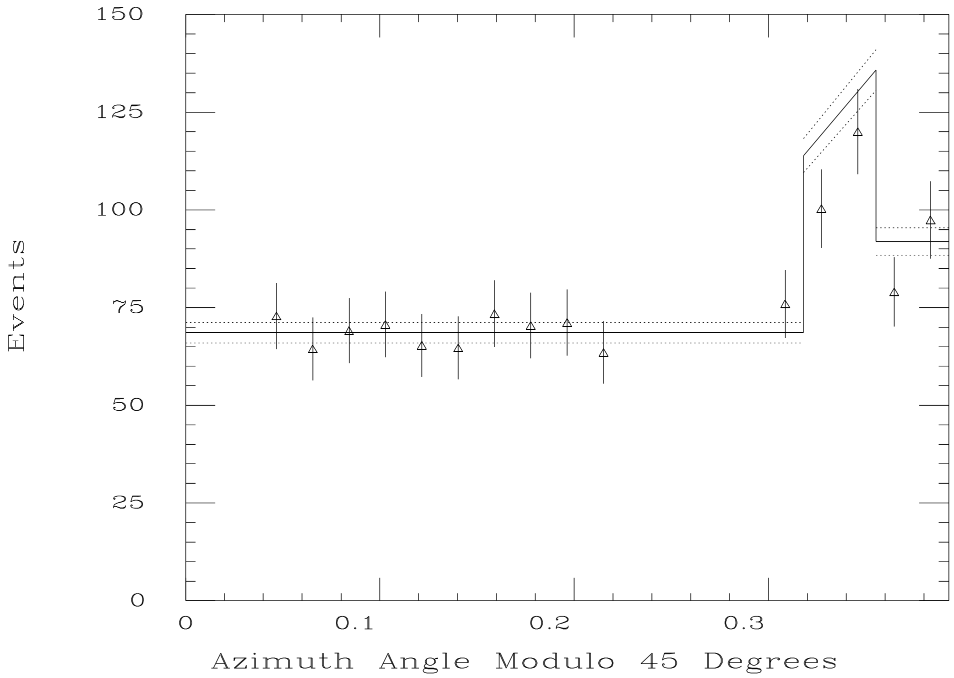

Figure 28: CDT hit rate versus azimuth angle modulo 45^0, in order to show the effect of the 8 reinforcement ribs in the CTC, which add more material. The solid line is the expected rate using the material estimate and the dotted lines indicate the uncertainty.

Background data samples of π^o , η and K_S^0 were generated and simulated including the effect of the Δz and $\widetilde{\chi^2}$ cut. The background efficiency was calculated using the above single photon hit efficiency and previously quoted particle fractions. The deviation of this estimate from a simple two photon model of the background hit efficiency, $\epsilon_{\pi^0} = 2\epsilon_\gamma - \epsilon_\gamma^2 = 0.181$, was taken to be the systematic uncertainty for the background hit rate. This difference ranged from .005 at low E_T to .011 at high E_T.

Figure 29 shows the observed conversion rate for the sample. Also indicated is the expected rate for background and single photons. These data and curves, together with equation 1, provide the basis for evaluating the number of isolated direct photon events.

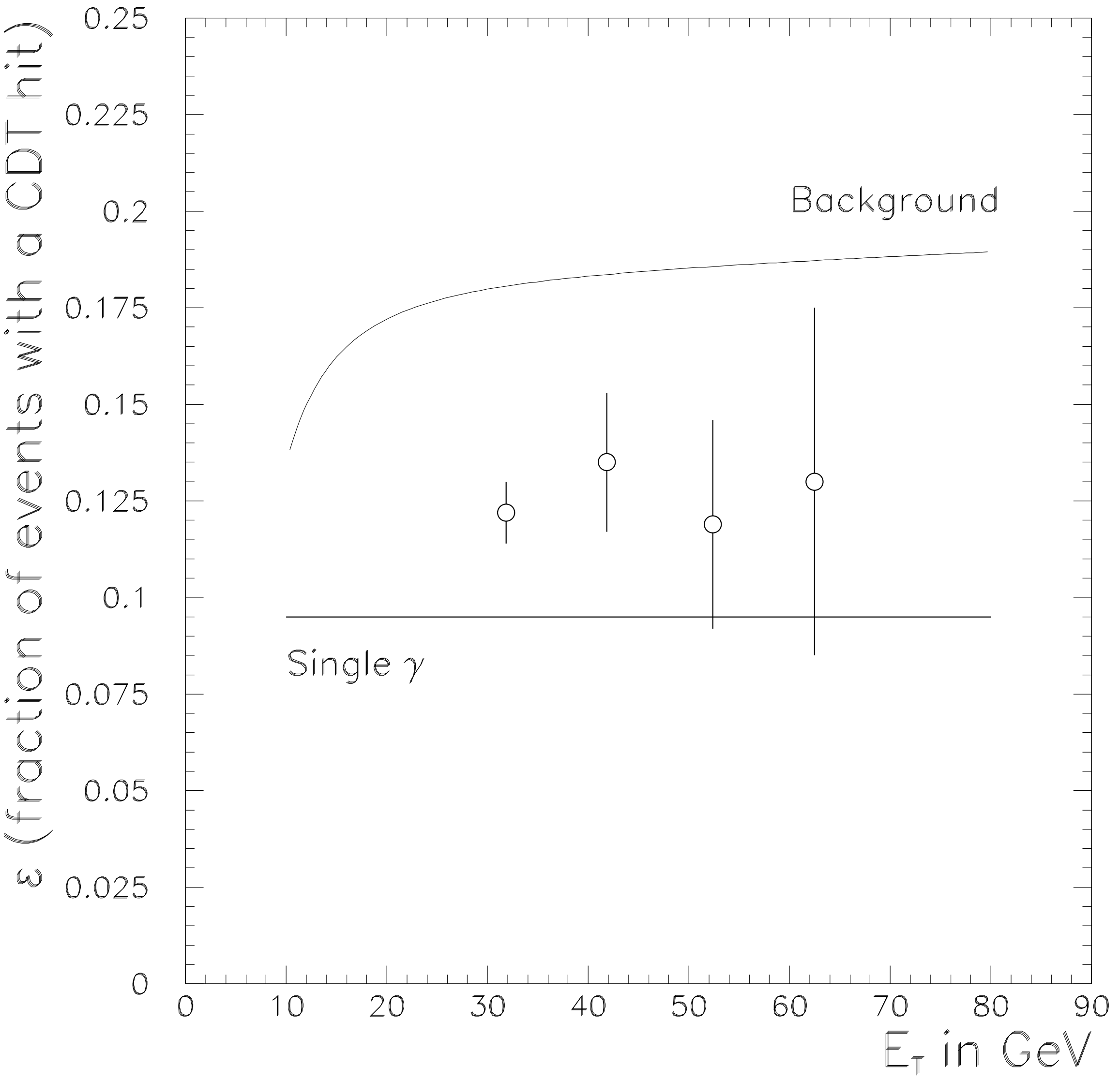

Figure 29: The expected CDT hit rate for background and single γ events (solid lines). The data points are the observed hit rate with errorbars indicating the systematic uncertainty.

7 Cross Section Evaluation and Systematic Uncertainties

The cross section was evaluated using the expression:

$$\frac{1}{\Delta\eta}\int_{-0.9}^{0.9}\frac{d^2\sigma}{dP_T d\eta}d\eta = \frac{N_\gamma}{\Delta P_T \Delta\eta \epsilon_{\rm cuts} L}. \tag{8}$$

N_γ is the number of prompt photons after background subtraction in the bin of width ΔP_T, and is evaluated as in equation 1. The quantity $\epsilon_{\rm cuts}$ is the total efficiency for the event and photon selection cuts listed in table 2 and table 3. L is the integrated luminosity, 3.28 $\rm pb^{-1}$ for the 23 GeV trigger and 102 $\rm nb^{-1}$ for the 10 GeV trigger. This luminosity was evaluated by using the observed beam-beam counter coincidence rate and a calculated total cross section for the beam-beam coincidence of 46.8 ± 3.2 mb [29]. The cross section is averaged over the pseudorapidity interval $|\eta| < 0.9$ giving $\Delta\eta = 1.8$.

We have evaluated the cross section and systematic uncertainties for two different choices of the isolation cut, in order to check theoretical predictions for the effect of this cut. The two choices are a fixed 2 GeV cut in a cone of 0.7 around the photon, and a fractional cut at 15 percent of the photon P_T in a cone of 0.7. The fixed cut is more stringent at high P_T, reducing the amount of background and the systematic uncertainties. Therefore it is our default choice, and all of the subsequent discussion is for this choice, unless otherwise noted.

The systematic uncertainties in the cross section are dominated by the uncertainties in the background subtraction. The systematic uncertainties in the background subtraction efficiencies are propagated to the measured number of photons by substituting into Equation 9 the systematic bounds on ϵ_γ and ϵ_b. To avoid having the statistical uncertainties on the measured value of ϵ propagate into the systematics, a smooth form of ϵ versus P_T from a quadratic fit is used. ϵ'_γ and ϵ'_b are the systematic bounds on the photon and background efficiencies, respectively, and N'_γ is the number of photons found with these limits. The fractional systematic bound in the number of photons is:

$$\frac{N'_\gamma}{N_\gamma} = \left(\frac{\epsilon - \epsilon'_b}{\epsilon'_\gamma - \epsilon'_b}\right) / \left(\frac{\epsilon - \epsilon_b}{\epsilon_\gamma - \epsilon_b}\right). \tag{9}$$

For the profile method, the percent systematic uncertainty in the number of photons, $100 \times ((N'_\gamma/N_\gamma) - 1)$, is shown in Figure 30 for each source of systematic uncertainty in the $\tilde{\chi}^2$ efficiency. For clarity, only the positive systematic uncertainties are shown; the negative uncertainties are similar. The uncertainties display a shallow minimum where the difference between the data efficiencies and background efficiencies is the greatest and rise with increasing P_T as that difference decreases. Since this behavior is fairly independent of the shape of the uncertainties on the efficiencies themselves, the uncertainties can be decomposed into a P_T dependent and a P_T independent systematic uncertainty by subtracting the minimum systematic uncertainty in quadrature for each source of uncertainty. Thus for each of the curves in Fig. 30 we find the minimum value of the uncertainty, $\sigma_{\rm ind}$, which is the P_T independent systematic uncertainty, and then for each point along the curve, σ, we subtract the minimum systematic uncertainty in quadrature to find the P_T dependent systematic uncertainty:

$$\sigma_{\rm dep} = \sqrt{\sigma^2 - \sigma_{\rm ind}^2}. \tag{10}$$

There are additional systematic uncertainties due to luminosity, P_T scale, and selection criteria efficiencies. The luminosity uncertainty is 6.8% [29]. The uncertainty in the P_T scale is the same as that of the W boson mass measurement [30], and is less than 1%. When this is convoluted with the falling spectrum the cross section uncertainty due to the P_T scale is 5%. All of our selection criteria efficiency uncertainties have been estimated/checked with $p\bar{p}$ data, and they are all less than approximately 1%. This is negligible compared to other uncertainties. The one analysis cut that has physics implications is the isolation cut. The number of photons that are lost due to the underlying event fluctuating above the isolation cut is corrected for. A sample of minimum bias collision events (events taken with no trigger except for a beam-beam counter coincidence) are used to measure the underlying event. This measurement has an uncertainty of about 1% (combined statistical and systematic), and is our estimate of the isolation cut uncertainty.

The systematic uncertainties for the conversion method are also dominated by the uncertainties in the background subtraction. The relative uncertainty in the conversion probability for a single photon is 18%. This gives a P_T independent systematic uncertainty of +31%(-45%), and P_T dependent systematic uncertainties of 6-8%. The uncertainty due to multiple π^0's (which give a larger conversion rate) was evaluated by comparing a background dominated sample (using the cut $\tilde{\chi}^2 > 8$) with our Monte Carlo background prediction. This uncertainty is negligible compared to the uncertainty in the single photon efficiency. The uncertainties on the luminosity, P_T scale, and analysis cuts are the same as the profile method quoted earlier.

The conversion method is statistically much weaker than the profile method. It is valuable in that it can be used at higher P_T than the profile method. In order to indicate the level of agreement of the two methods at all P_T values, we calculate the expected conversion rate in the CDT, based on the profile method results. That is we take the ratio measured using the profile method of signal to background, and combine it with the expected conversion rates of signal and background in the CDT, and predict the total(signal+background) conversion rates. This is shown in Fig. 31. At lower P_T the conversion rate is consistent with the rate expected using the background estimates from the profile method, but it does not add significantly to our measurement. For this reason only the data above 28 GeV has been used for the cross section measurement with the conversion method.

Figure 32 shows the final direct photon cross section for the profile method and the conversion method, and the results are tabulated in table 4. Included in table 4 is the number of events that contribute to each cross section point and the number of photons after background subtraction (there is no correction for event losses). The profile method (first 11 points) has an additional normalization uncertainty of 27%. The conversion method (last 4 points) has a +32%(-46%) normalization uncertainty.

We now compare the results from the different isolation cuts, as mentioned earlier. The

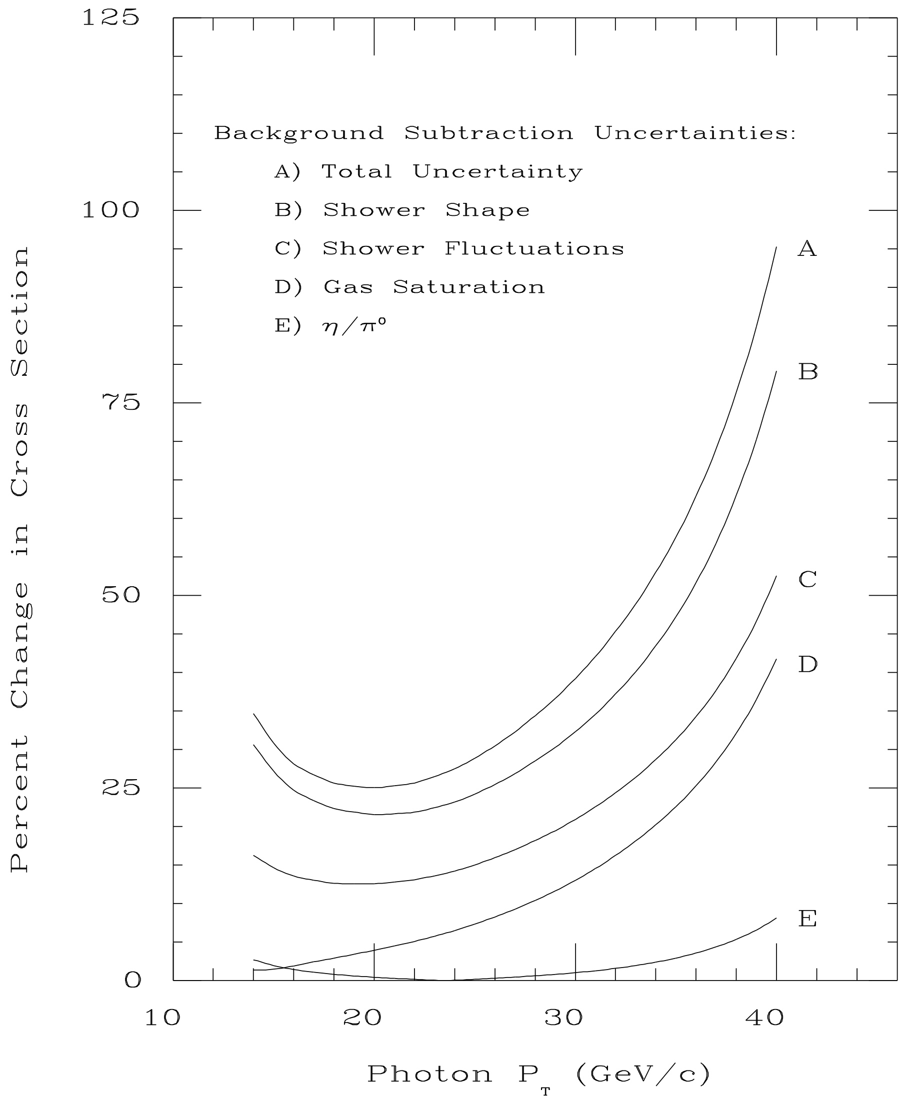

Figure 30: Percent change in the photon cross section for the profile method due to uncertainties in the background subtraction method. (Only the positive systematic uncertainties are shown.)

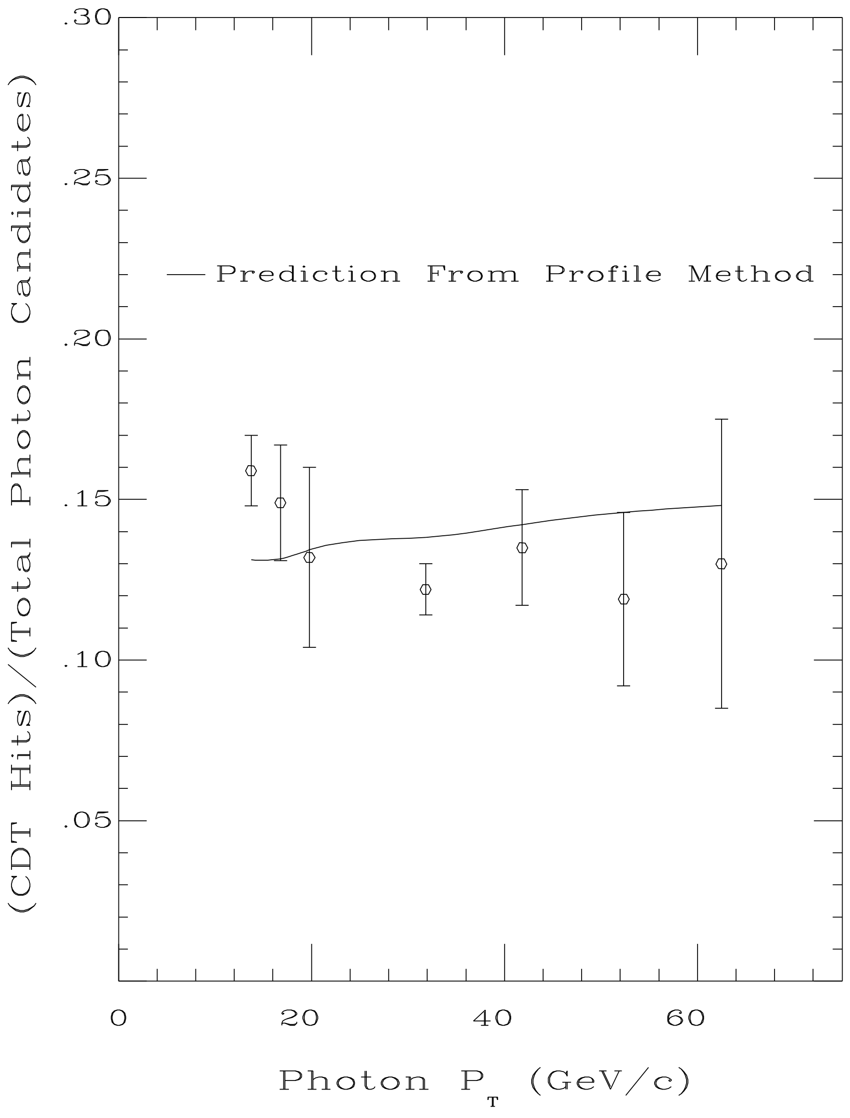

Figure 31: The hit rate observed in the CDT (points) for events with $\tilde{\chi}^2 < 8$ compared to the expected hit rate using the backgrounds evaluated with the profile method (smooth curve).

P_T Bin (GeV/c)	P_T (GeV/c)	# Events	# Photons	$d^2\sigma/dP_Td\eta$ (pb/(GeV/c))	Stat. (%)	Sys. (%)
$14-15$	14.5	612	263	3.16×10^3	11	21
$15-17$	15.9	691	253	1.55×10^3	12	13
$17-19$	17.9	338	177	1.03×10^3	13	6
$19-22$	20.4	250	108	4.36×10^2	18	2
$22-27$	24.0	156	79	1.91×10^2	22	12
$27-28$	27.5	529	307	1.30×10^2	12	23
$28-29$	28.5	417	272	1.13×10^2	12	26
$29-31$	30.0	721	381	7.15×10^1	12	32
$31-33$	32.0	503	344	6.98×10^1	11	40
$33-35$	34.0	364	185	3.78×10^1	20	50
$35-40$	37.3	594	266	2.23×10^1	20	71
$28-38$	32.2	2137	1466	6.05×10^1	15	7
$38-48$	42.4	522	279	1.19×10^1	37	6
$48-58$	52.5	199	143	6.53×10^0	41	6
$58-68$	62.6	77	46	2.22×10^0	79	8

Table 4: The cross section calculated using the profile and conversion methods is tabulated along with the statistical uncertainty and the P_T dependent component of the systematic uncertainty. This cross section uses the isolation cut of 2 GeV in a cone around the photon. An additional normalization systematic uncertainty of 27% is common to the first 11 entries, while a normalization uncertainty of +32%(-46%) is common to the last 4 entries.

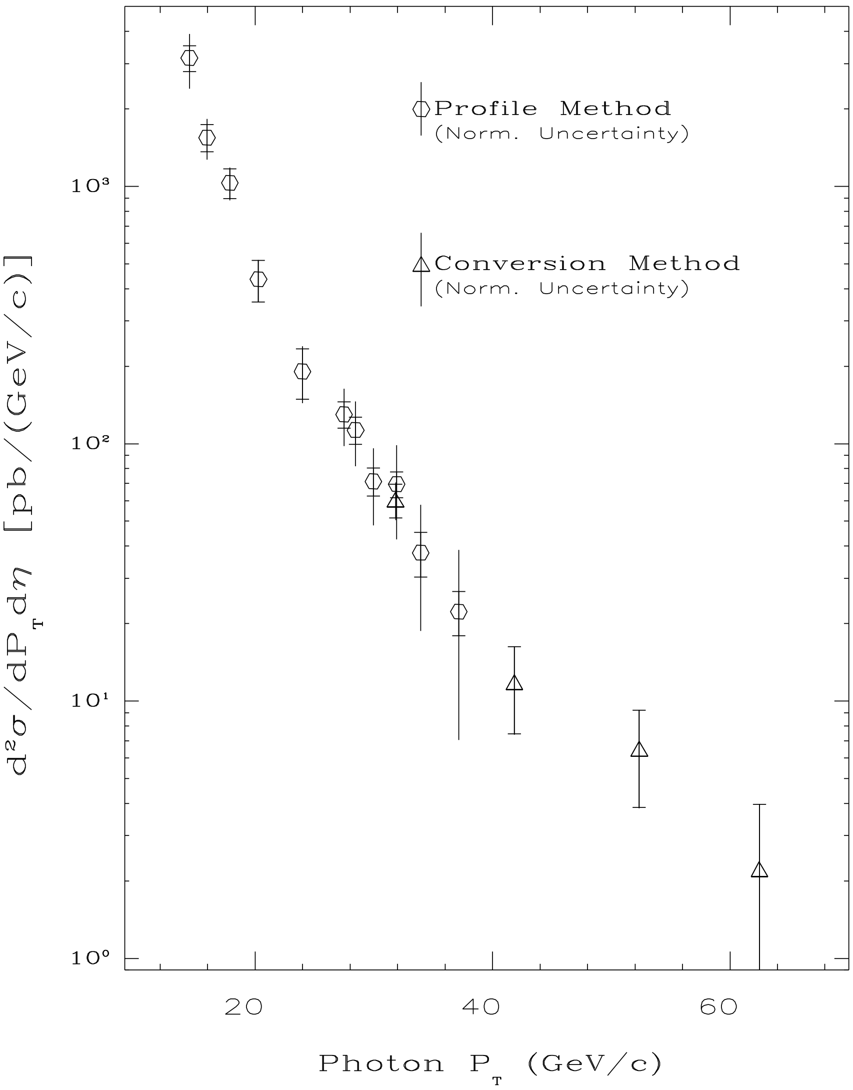

Figure 32: The direct photon cross section from the profile method and the conversion method.

cross section from the fractional 15% cut is tabulated in table 5. An additional normalization systematic uncertainty of 29% is common to the first 11 entries, while the normalization uncertainty of +42%(-61%) is common to the last 4 entries. Both measurements are described well by a function of the form $A/{P_T}^5$, with the best fit for A being 2.03×10^9 pb. Figure 33 compares the two results by multiplying both cross sections by ${P_T}^5$, and dividing by A. This shows that the two cross sections are consistent with each other, the theoretical prediction for these results is shown in the next section. The increase in the measurement uncertainties with the less restrictive 15% cut is also evident.

P_T Bin (GeV/c)	P_T (GeV/c)	$d^2\sigma/dP_T d\eta$ (pb/(GeV/c))	Stat. (%)	Sys. (%)
$14-15$	14.5	3.04×10^3	12	16
$15-17$	15.9	1.67×10^3	12	9
$17-19$	17.9	1.11×10^3	13	4
$19-22$	20.4	4.92×10^2	18	6
$22-27$	24.0	2.53×10^2	19	17
$27-28$	27.5	1.50×10^2	11	30
$28-29$	28.5	1.38×10^2	11	34
$29-31$	30.0	8.04×10^1	12	41
$31-33$	32.0	6.83×10^1	13	51
$33-35$	34.0	3.27×10^1	26	63
$35-40$	37.3	2.64×10^1	18	89
$28-38$	32.2	6.31×10^1	16	6
$38-48$	42.4	1.59×10^1	32	6
$48-58$	52.5	8.71×10^0	33	8
$58-68$	62.6	1.71×10^0	121	15

Table 5: The cross section calculated using the profile and conversion methods is tabulated along with the statistical uncertainty and the P_T dependent component of the systematic uncertainty. This measurement uses an isolation cut of 15% of the photon P_T in a cone around the photon. An additional normalization systematic uncertainty of 29% is common to the first 11 entries, while a normalization uncertainty of +42%(-61%) is common to the last 4 entries.

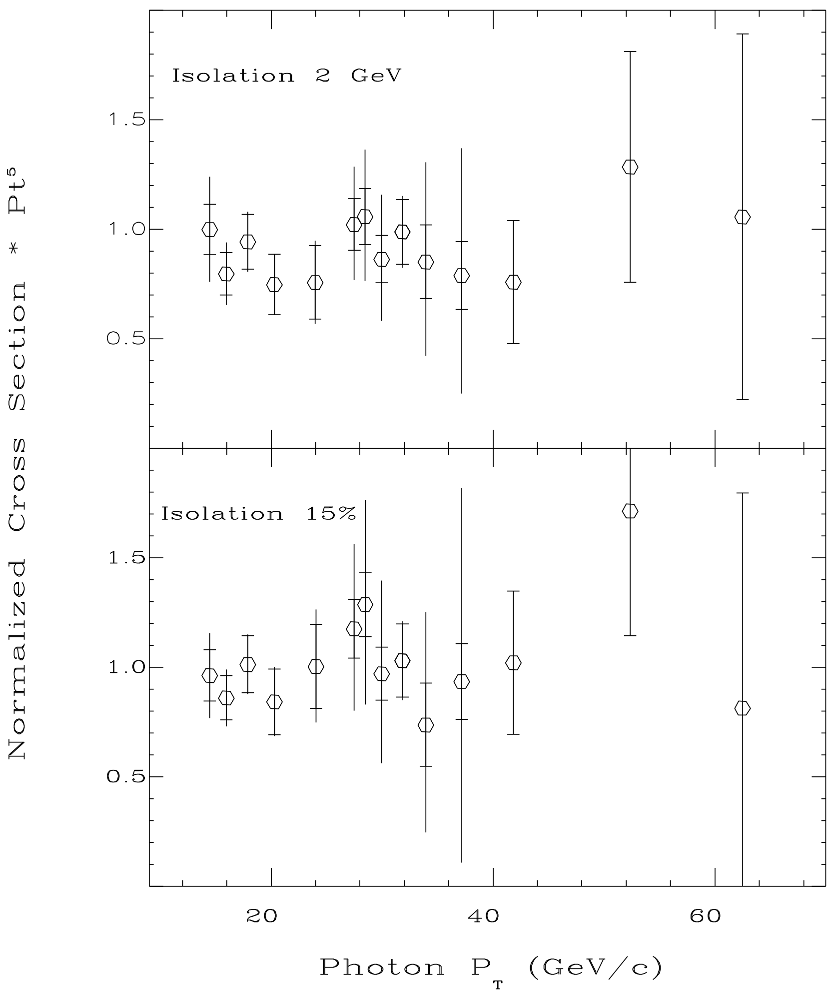

Figure 33: The combined direct photon cross sections for two different choices of the isolation cut, a fixed 2 GeV cut, and a fractional 15% cut. Both cross sections are scaled by ${P_T}^5$.

8 Comparison with QCD Predictions

The cross section measurement can now be compared with QCD calculations to see how well the data and underlying theory can constrain parton distributions, particularly the gluon distribution. The predictions used are those provided by J.F. Owens, described in Baer et al. [31], and P. Aurenche, described in Aurenche et al. [11]. Both calculations utilize next-to-leading order matrix elements, and include the contribution from bremsstrahlung photons and the effect of an isolation cut. The effects of various theoretical uncertainties will be explored, including the uncertainty on the calculation of the *bremsstrahlung* process and the effects of the isolation cut on it, the uncertainty due to the choice of scales in the calculation, and the parton distributions.

Figure 34 shows the comparison between our measured cross section and the QCD prediction we use as the standard for all subsequent plots. This prediction uses the program of Owens with KMRS $B_0 - 190$ ($\Lambda = 190$) parton distributions [32]. There are three calculation scales to be chosen. The renormalization scale μ_R is used in the evolution of α_s, the factorization scale μ_F is that used in the parton distribution evolution, and the photon fragmentation function scale μ_f is used in the fragmentation functions for the *bremsstrahlung* process. We choose all three scales to be the photon P_T. This calculation uses an isolation cut of 1.6 GeV in a cone of radius 0.7 around the photon. The 1.6 GeV cut is the value best matched to the data cut of 2.0 GeV(the 2.0 GeV included +.86 GeV of underlying event and -.46 GeV of detector energy losses). There is general agreement between the data and the theory over three orders of magnitude in cross section, but the data has a steeper slope at low P_T. This is also true for data from the CERN $\bar{p}p$ Collider ($\sqrt{s}$=630 GeV) [33], which is shown in Fig. 34 as well.

The visual comparison between data and theory is aided by plotting (data-theory)/theory on a linear scale. The following six comparisons with QCD are of this type for a wide variety of theoretical predictions. Conclusions from these comparisons are presented after the entire set of predictions are shown. The default theory is described above and shown in Fig. 34. This is represented by the dashed line at 0.0 in each figure (unless noted otherwise).

The first set of predictions are displayed in Fig. 35 for three different choices of μ_R, μ_F and μ_f. Once again the data and theory generally agree, but the slope of the data at low P_T is steeper than the theory. To investigate the theoretical uncertainty due to scale choices we use the Aurenche program, which has the option of determining the "optimized" scale [15]. The MT-B1 parton distributions [34] are used for all of the Aurenche predictions in this plot. The three solid curves are as labelled $\mu = P_T$, $\mu = 2P_T$, $\mu = optimized$. The $\mu_R = \mu_F = \mu_f = P_T$ calculations are 8% higher (P_T independent) than the corresponding $\mu_R = \mu_F = \mu_f = 2P_T$ calculations. The optimization procedure leads to scales of $\mu_R \approx P_T/7, \mu_F = \mu_f \approx 7P_T$. The optimized scales lead to systematically larger cross sections, but the cross section does not rise at lower P_T as rapidly as the data.

The dependence of the theoretical prediction on the isolation cut and the associated *bremsstrahlung* diagram leads to three sources of uncertainty. First, the calculation uses the leading order prediction for the two-jet cross section from which the *bremsstrahlung*

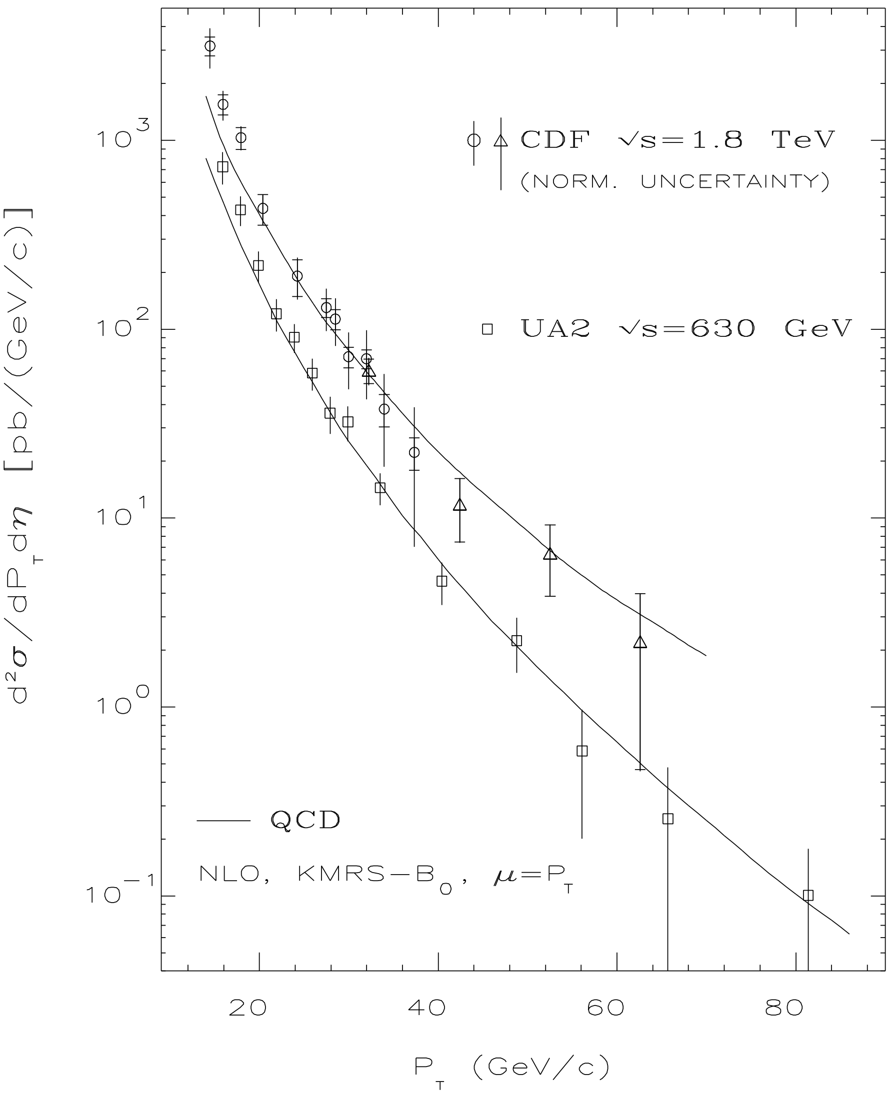

Figure 34: The isolated direct photon cross section, from both CDF and UA2, compared to a recent QCD prediction described in the text.

photon originates. Second, the photon fragmentation function is only calculated to leading order, and has never been measured. Finally, the isolation cut in the theory is always an approximation of what is used in the data. The parameters of the prediction are varied to estimate the possible size of these effects. Figure 36 shows the default prediction with the cone 0.7 isolation cut, as represented by the dashed line. Also shown is the prediction with a cone of 0.4 with very little change in the resulting cross section. Varying the amount of energy in the cone in the prediction has also been tested, but is not shown, and also results in very small changes in the cross section. For example, doubling the cone energy to 3.2 GeV increases the cross section by 5%. Finally the prediction with the isolation cut completely removed is shown. This may seem too extreme given that the data does have an isolation cut, but it indicates the relative effect of the *bremsstrahlung* process. The size of this change is also typical of the cross section differences in preliminary calculations of higher order corrections to the *bremsstrahlung* process [17]. These calculations have not taken into account the isolation cut as yet and therefore are not shown.

The theoretical prediction is also sensitive to choices of parton distributions. We present four different sets of parton distributions to illustrate this. The first set is "MRS B_0", from reference [35], which varies the gluon distribution by limits defined by fixed target direct photon data [36]. The second set of parton distributions is from "KMRS B", from reference [32], where the form of the gluon distribution is altered and the effects of QCD shadowing are explored. The third set of parton distributions is "HMRS E", from reference [37], which uses different data for the quark distributions and also varies the form of the gluon distribution. The final set of parton distributions is from Morfin-Tung, "MT", from reference [34], which independently fits the data sets used in the MRS sets. These four sets do not include recent preliminary fits to new deep inelastic scattering data [38], nor fits including CDF b quark cross sections [39]. Calculations using these new fits were not available at the time of this publication.

Figure 37 demonstrates the differences in gluon distributions, $xG(x)$, from a sample of the four parton distribution sets, all relative to KMRS B_0-190. The scale used is $\mu = x \times 900$, which is the approximate central photon P_T. The x range covered by the present measurement is $\approx .015 - .07$, and significant differences are seen in the gluon distributions. Differences are also seen in the quark distributions, $xQ(x)$, shown in Fig. 38 for the same sample sets. These differences are mostly due to the sea quarks, which are correlated with changes in the gluon distributions.

The QCD predictions with these parton distribution sets are now compared to the data. The default prediction with KMRS B_0-190 parton distributions is shown again in Fig. 39 (dashed line), along with calculations using MRS B_0-200 and MRS B_0-160. The scales and isolation cuts are the same for the three predictions. Reference [35] also contains parton distribution sets MRS B_0-135 and MRS B_0-235. These are not shown since they only change the normalization of the curves, and do not change the shape significantly. Figure 40 shows the predictions using reference [32] parton sets, and the associated change in cross section is minimal. Figure 41 displays all of the calculations using parton distributions from reference [37], and the agreement with the data is generally worse than the other sets of parton

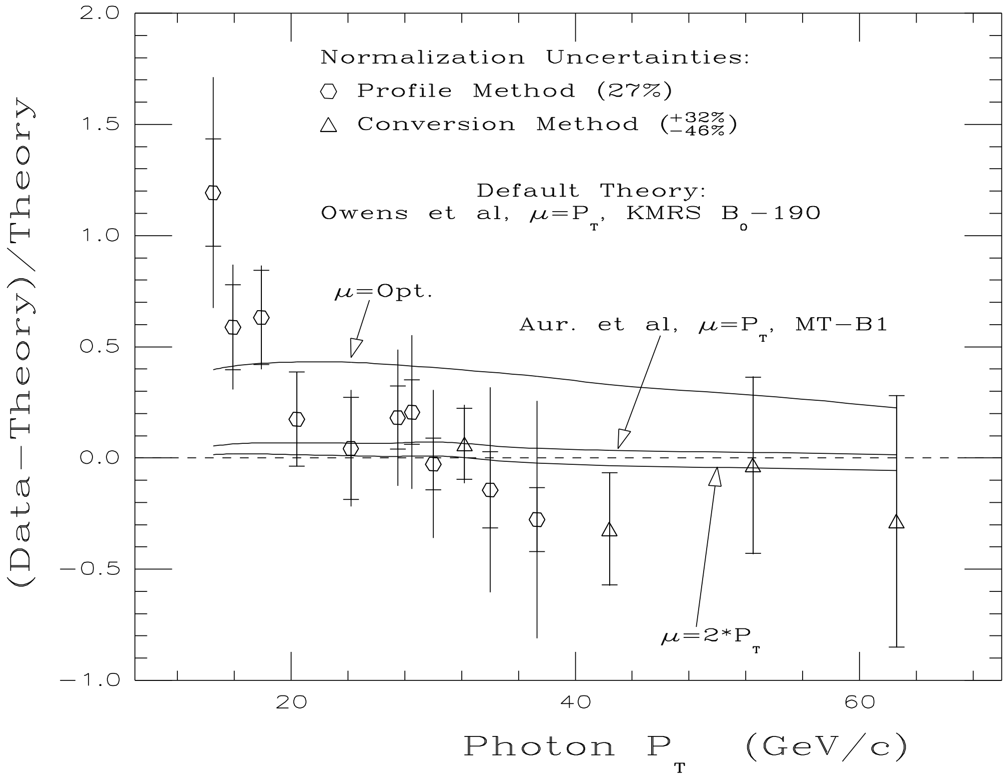

Figure 35: The choice of scale is varied in the QCD predictions, and compared to the data.

distributions. Finally the predictions using the parton sets of reference [34] and the Aurenche program are shown in Fig. 42, with similar results as the other sets. The set MT-S1 is not plotted because it gave predictions very similar to our default calculation.

Several conclusions may be drawn from these comparisons. The first conclusion is that the data give a qualitative agreement with the QCD predictions over a wide range in P_T. However, the slope of the data at low P_T is not reproduced by the theory, no matter what choice of theoretical parameters or parton distributions are used. The second conclusion is that the present uncertainties in the data are comparable to the variation of the theory with different parton distributions, making it difficult to constrain them even if there were no theoretical uncertainty. Finally, the theoretical uncertainties at present, based on variations of scale and the treatment of *bremsstrahlung* photons, are as large as those due to parton distributions, making the constraint of parton distributions with the inclusive cross section very difficult.

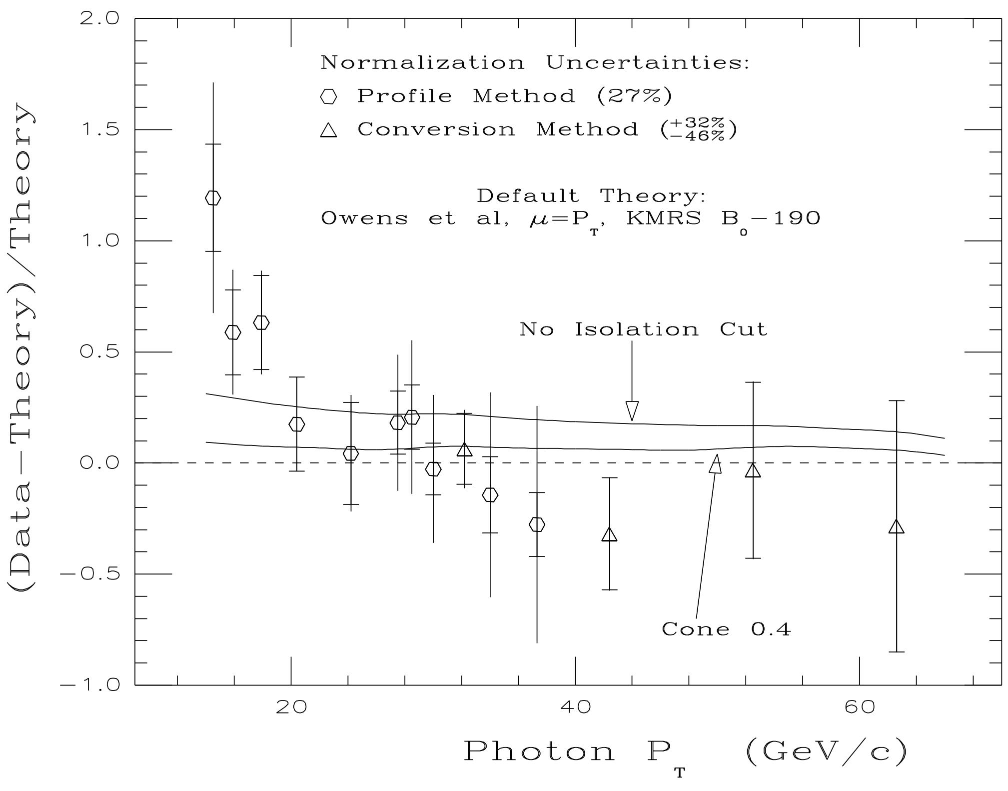

Figure 36: The parameters in the QCD prediction related to the *bremsstrahlung* process and the isolation cut are varied, and compared with the measurement.

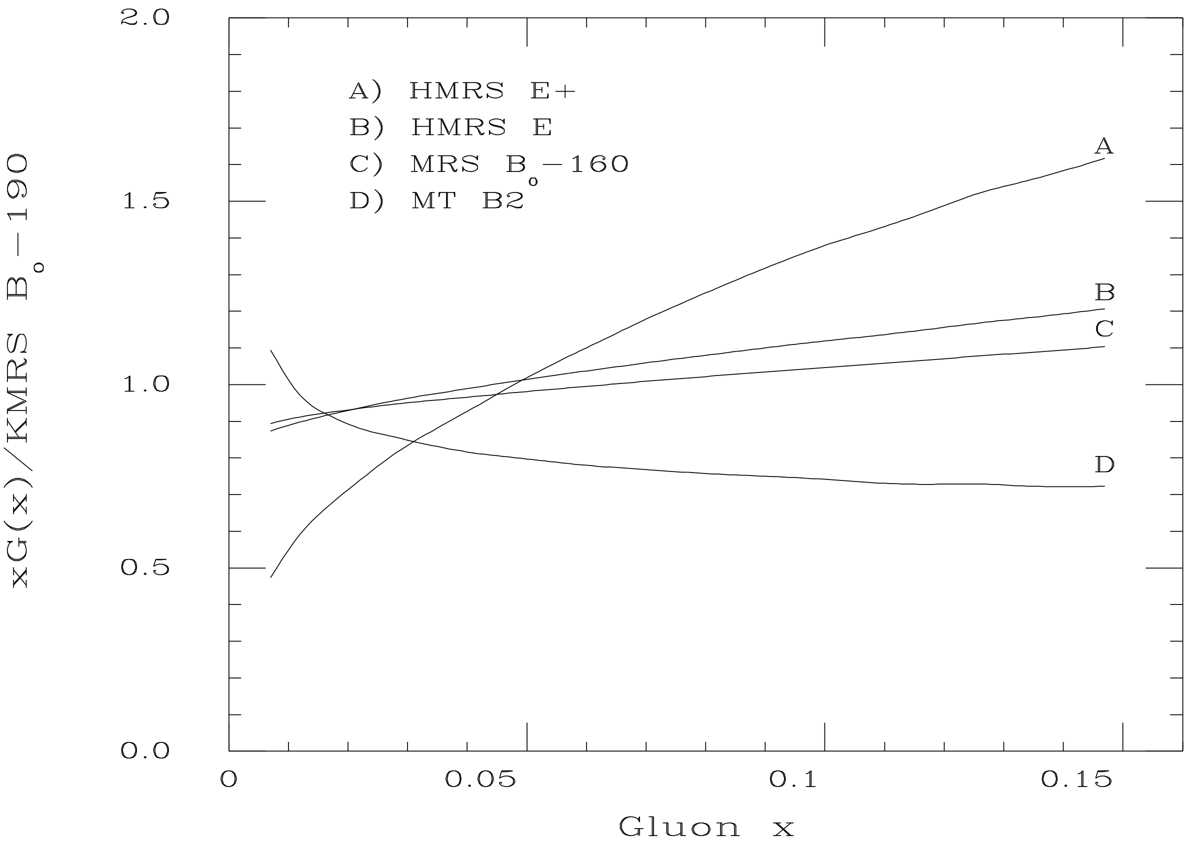

Figure 37: The different gluon distributions are compared, relative to the default KMRS B_0-190.

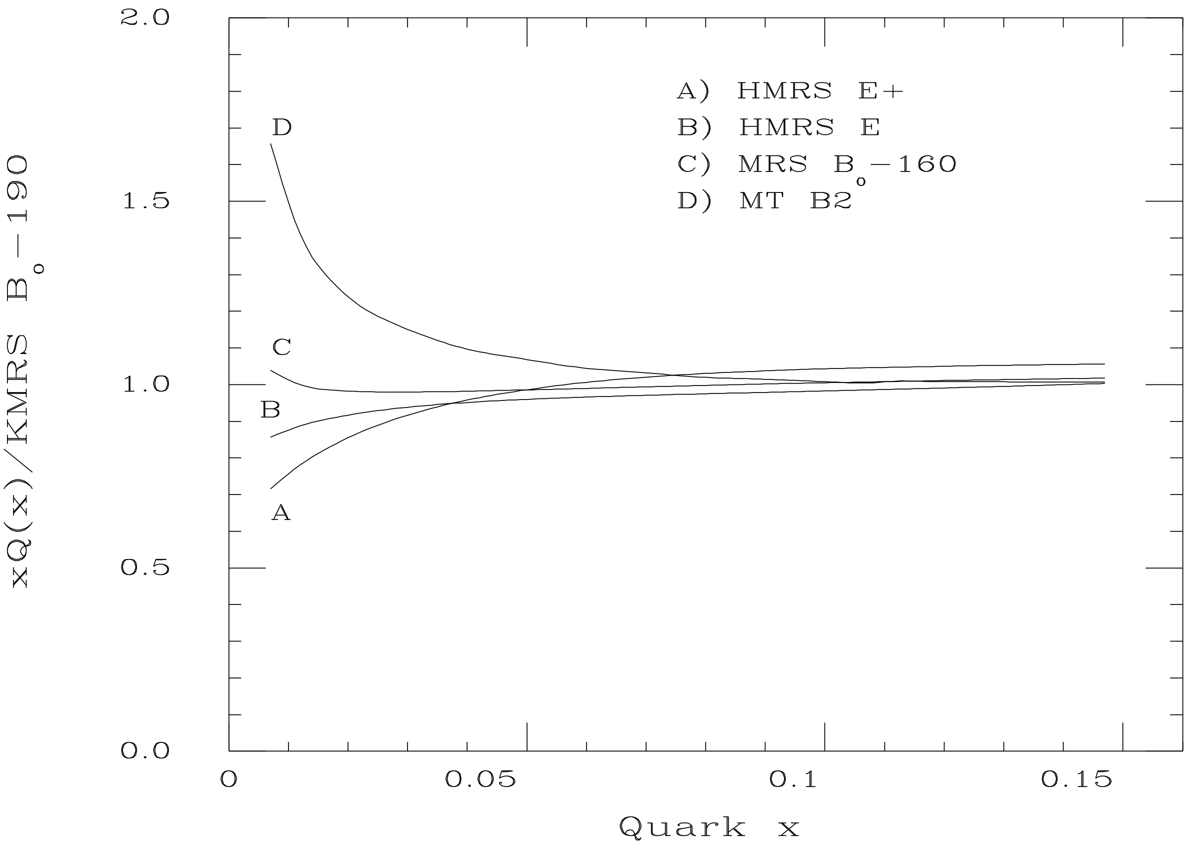

Figure 38: The different quark distributions are compared, relative to the default KMRS B_0-190.

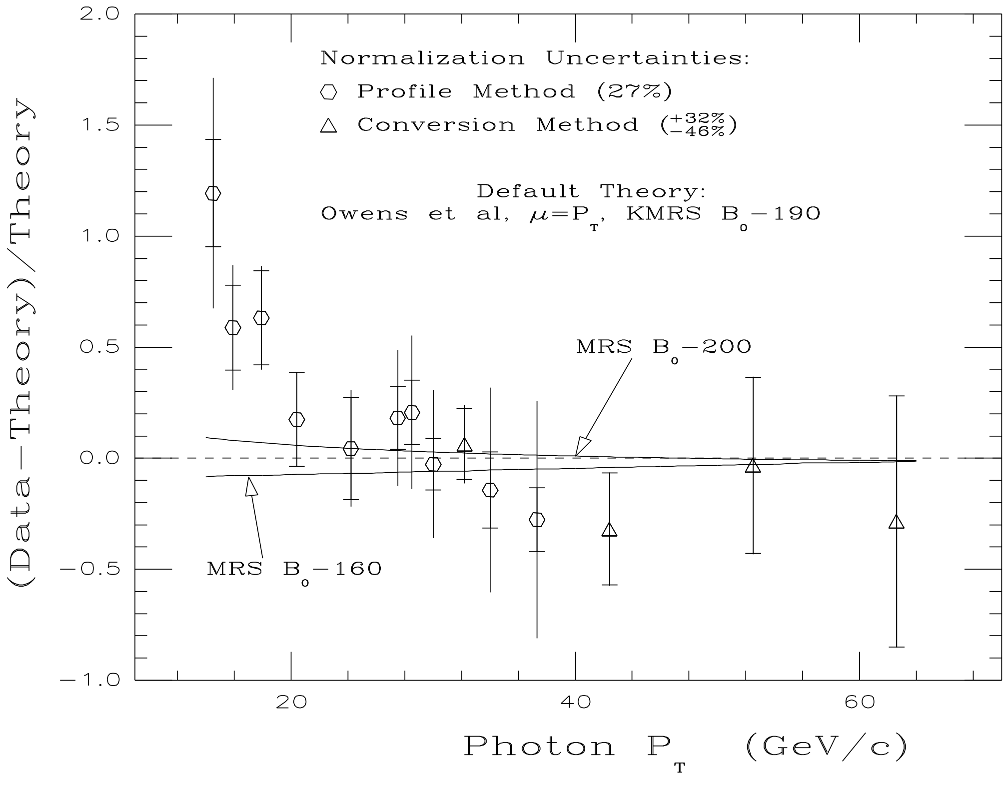

Figure 39: The input sets of parton distributions from reference [35] are varied in the QCD prediction, and compared with the data.

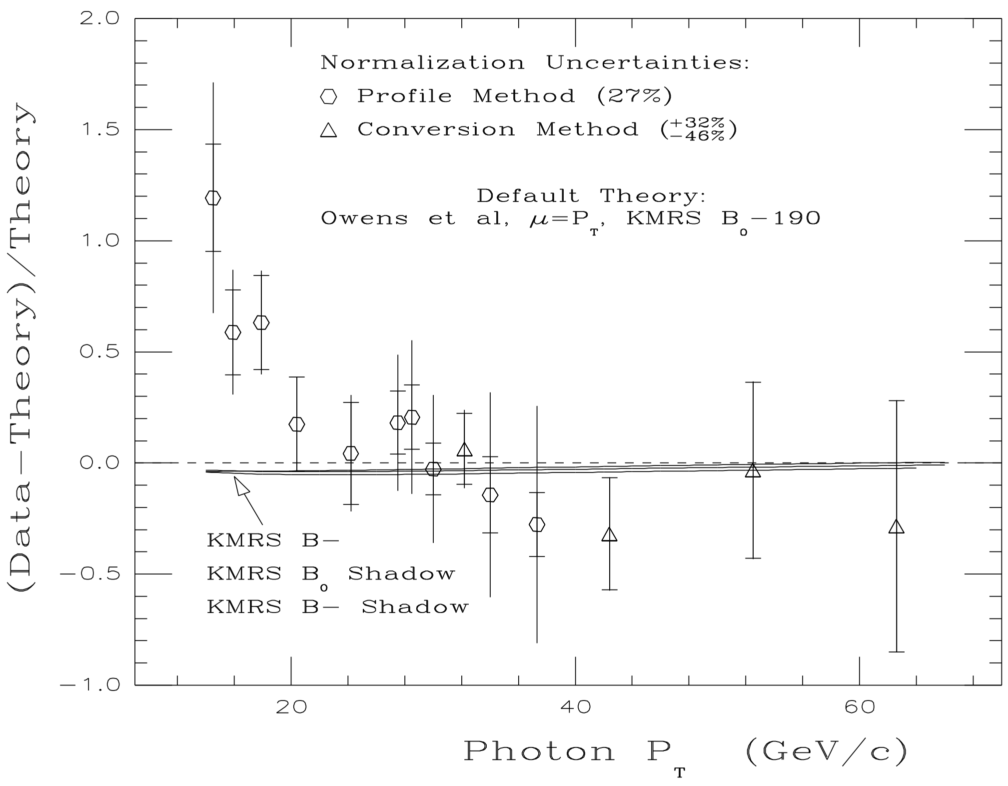

Figure 40: Reference [32] parton distribution sets are varied in the QCD prediction, and compared with the CDF measurement.

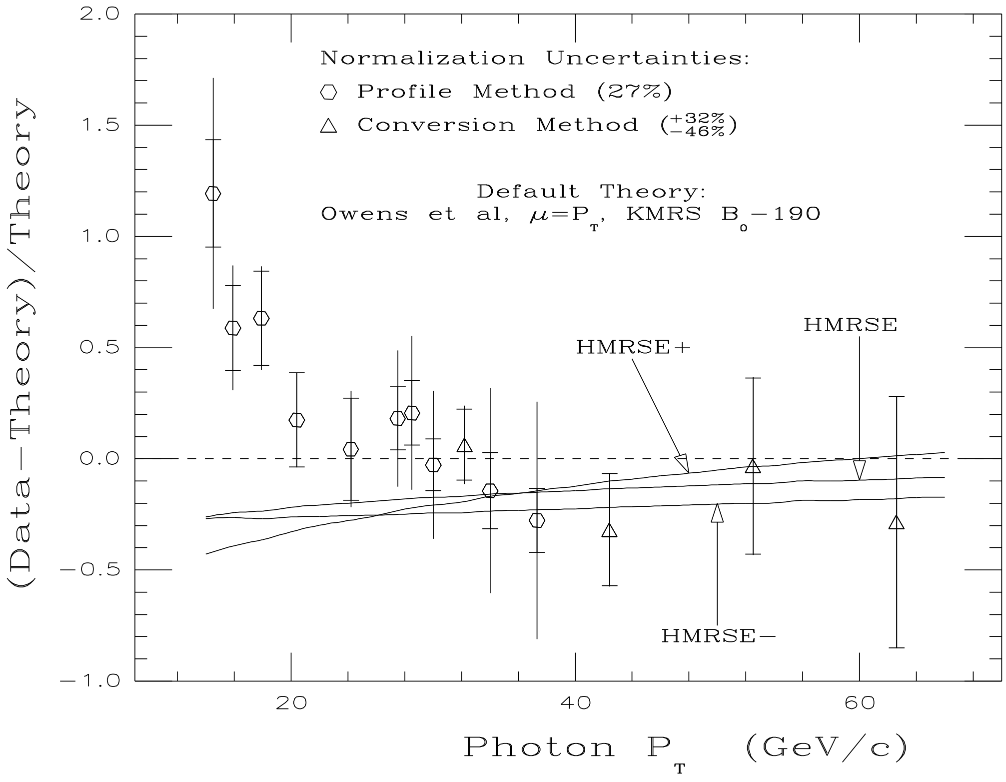

Figure 41: The input sets of parton distributions from reference [37] are varied in the QCD prediction, and compared with the CDF data.

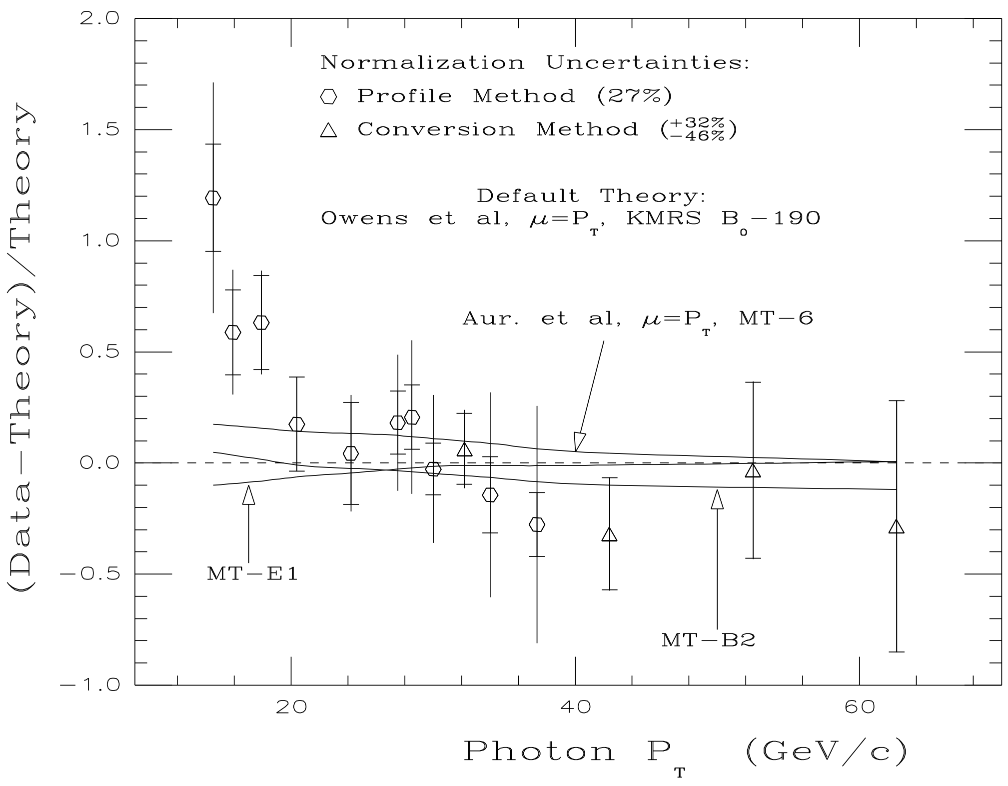

Figure 42: Reference [34] parton distribution sets are varied in the QCD prediction, and compared with the CDF measurement.

9 Summary

The first prompt photon cross section measurement at the Fermilab Tevatron Collider has been presented. The details of the event selection, detector simulation, and background subtraction have been described. Cross checks of the two independent background subtraction methods have been made from the data, and demonstrate the accuracy of our detector simulation and other aspects of the analysis. The data has been compared to QCD predictions that span the range of parton distributions and theory parameters. Most of these predictions give a qualitative agreement with the data, but none of the predictions investigated reproduce the slope of the measured cross section at low P_T.

10 Future Prospects

The interest in prompt photon production is due to the clean identification of the photon, and the gluon-dominated production processes. This leads to the obvious goal of a test of modern sets of parton distributions, particularly the gluon distribution, and a precise test of QCD. A more direct *measurement* of the gluon distribution is possible in the future by studies of the kinematics of the photon plus jet system, but here we test QCD and the parton distributions with the inclusive cross section. The present measurement has tested a previously unexplored center-of-mass energy and x_T region, and gives a qualitative agreement with QCD, but has a steeper slope at low P_T. As we have seen, the present uncertainties in the measurement, both statistical and systematic, are comparable to or somewhat smaller than the differences between modern parton distributions, making comparisons possible but somewhat inconclusive. Future improvement in these uncertainties with more data and an upgraded central photon detector will certainly improve this situation. The CDF central detector has been fitted with preshower chambers between the solenoid and the central electromagnetic calorimeter for the 1992 Tevatron collider running period. These chambers will provide the same conversion probability technique as was used in this paper, but with a more optimal, approximately one radiation length, radiator provided by the coil and cryostat. This should allow a reduction in the systematic uncertainties in the measurement, perhaps by as much as a factor of three. We have also seen that the present theoretical uncertainties in the choice of scale and the *bremsstrahlung* process are comparable to or larger than the differences between modern parton distributions. This makes the constraint of parton distributions very difficult. Future improvement in this situation would be welcome.

Acknowledgements

We thank the Fermilab staff and the technical staffs of the participating institutions for their vital contributions. This work was supported by the U.S. Department of Energy and National Science Foundation; the Italian Istituto Nazionale di Fisica Nucleare; the Ministry of Science, Culture, and Education of Japan; and the A. P. Sloan Foundation.

References

[1] H. D. Politzer. *Physical Review Letters*, 30(26):1346, 1973.

[2] D. J. Gross and F. A. Wilczek. *Physical Review Letters*, 30(26):1343, 1973.

[3] H. Fritzsch, M. Gell-Mann, and H. Leutwyler. Advantages of the color octet gluon picture. *Physics Letters*, B(47):365, 1973.

[4] R. P. Feynman. Very high-energy collisions of hadrons. *Physical Review Letters*, 23:1415, 1969.

[5] R. Field and R. Feynman. A parameterization of the properties of quark jets. *Nuclear Physics*, B(136):1, 1977.

[6] G. Altarelli and G. Parisi. *Nuclear Physics*, B(126):298, 1977.

[7] A.D. Martin, R.G. Robert, and W.J. Stirling. *Physical Review*, D(37):1161, 1988.

[8] E. Eichten, I. Hinchliffe, K. Lane, and C. Quigg. *Reviews of Modern Physics*, 56:579, 1984.

[9] D. Duke and J. F. Owens. *Physical Review*, D(30):49, 1984.

[10] M. Diemoz, F. Ferroni, E. Longo, and G. Martinelli. *Zeitschrift fur Physik*, C(39):21, 1988.

[11] M. Fontannaz, P. Aurenche, R. Baier and D. Schiff. Prompt photon production at large p_t scheme invariant QCD predictions and comparison with experiment. *Nuclear Physics*, B(297):661, 1988.

[12] T. Akesson *et al.* (The Axial Field Spectrometer collaboration). Direct-photon plus away-side jet production in pp collisions at $\sqrt{s} = 63$ GeV and a determination of the gluon distribution. *Zeitschrift fur Physik*, C(34):293, 1987.

[13] E. Braaten, E.L. Berger and R.D. Field. *Nuclear Physics*, B(239):52, 1984.

[14] Edmond L. Berger and Jianwei Qiu. Calculations of Prompt Photon Production in QCD. *Physical Review*, D(44):2002, 1991.

[15] M. Fontannaz, P. Aurenche, R. Baier and D. Schiff. Dealing with ambiguities in higher order QCD predictions for large p_t processes involving real photons. *Nuclear Physics*, B(286):509, 1987.

[16] J. Owens. *Reviews of Modern Physics*, 59(2):465, 1987.

[17] P. Aurenche *et al.* *Next to Leading Order Bremsstrahlung Contribution to Prompt-Photon Production*, May 1992. ENSLAPP-A-386/92.

[18] F. Abe *et al.* (CDF Collaboration). *Nuclear Instruments and Methods*, A(271):387, 1988.

[19] F. Snider *et al. Nuclear Instruments and Methods*, A(268):75, 1988.

[20] F. Bedeschi *et al. Nuclear Instruments and Methods*, A(268):50, 1988.

[21] S. Bhadra *et al. Nuclear Instruments and Methods*, A(268):92, 1988.

[22] L. Balka *et al. Nuclear Instruments and Methods*, A(267):272, 1988.

[23] J.A. Appel *et al.* (UA2 collaboration). Direct photon production at the CERN $p\overline{p}$ collider. *Physics Letters*, B(176):239, 1986.

[24] D. Amidei *et al. Nuclear Instruments and Methods*, A(267):51, 1988.

[25] R. Brun *et al. GEANT3*. CERN DD/EE/84-1.

[26] Particle Data Group. *Physics Letters*, B(239):III.15, 1990.

[27] R. G. Wagner (unpublished). based on calculations by F. Berends *et al.*, Z. Phys. C (27):155, 1985; F. Berends and R. Kleiss, Z. Phys. C (27):365, 1985.

[28] M. Schub. PhD thesis, Purdue University, 1989. unpublished.

[29] F. Abe *et al. Physical Review D*, 44(1):29, 1991.

[30] F. Abe *et al. Physical Review D*, 43(7):2070, 1991.

[31] J. Ohnemus, H. Baer and J.F. Owens. *Physical Review D*, 42(1):61, 1990.

[32] W.J. Stirling, J. Kwiecinski, A.D. Martin and R.G. Roberts. *Physical Review D*, 42(11):3645, 1990.

[33] J. Alitti *et al.* (UA2 collaboration). *Physics Letters*, B(263):544, 1991.

[34] J.G. Morfin and W.K. Tung. *Zeitschrift fur Physik*, C(52):13, 1991.

[35] R.G. Roberts, A.D. Martin and W.J. Stirling. *Physical Review D*, 43(11):3648, 1991.

[36] M. Bonesini *et al.* (WA70 Collaboration). *Zeitschrift fur Physik*, C(38):371, 1988.

[37] W.J. Stirling, P.N. Harriman, A.D. Martin and R.G. Roberts. *Physics Letters B*, 243(4):421, 1990.

[38] W. J. Stirling, A. D. Martin and R. G. Roberts. *New Information on Parton Distributions*, May 1992. RAL-92-021.

[39] Ruibin Meng, Edmond L. Berger and Wu-Ki Tung. *Implications of Bottom Quark Cross Section Data at Hadron Collider Energies*, April 1992. ANL-HEP-PR-92-32.